STUDY OF TWO-WAY COUPLED PARTICLE LADEN TURBULENT FLOW OVER A BACKWARD-FACING STEP USING LARGE-EDDY SIMULATION

By

Timothy M. Johnston

Reetesh Ranjan
Assistant Professor
(Advisor)

Kidambi Sreenivas
Professor
(Committee Member)

Trevor Elliott
UC Foundation Associate Professor
(Committee Member)

Abdollah Arabshahi
Research Professor
(Committee Member)

STUDY OF TWO-WAY COUPLED PARTICLE LADEN TURBULENT FLOW OVER A BACKWARD-FACING STEP USING LARGE-EDDY SIMULATION

By

Timothy M. Johnston

A Thesis Submitted to the Faculty of the University of
Tennessee at Chattanooga in Partial
Fulfillment of the Requirements of the Degree
of Master of Engineering

The University of Tennessee at Chattanooga
Chattanooga, Tennessee

December 2021

ABSTRACT

Large-eddy simulation (LES) is a computationally viable strategy to study particle-laden turbulent flows in practically relevant configurations, although modeling challenges need to be addressed for improved predictive capabilities. In this study, we perform a comprehensive assessment of subgrid-scale (SGS) models for LES by considering a two-way coupled particle-laden turbulent flow over a backward-facing step. We consider dynamic eddy viscosity, wall-adapting local eddy viscosity (WALE), and dynamic one-equation models for the closure of the SGS stress tensor, and the random walk (RW) and the differential filter (DF) based models for the subgrid dispersion. The assessment of subgrid models is carried out by comparison of simulation results against the available experimental data. Based on the assessment studies, the WALE model for the SGS stress tensor and the RW model for the subgrid dispersion are considered to examine the effects of inertia, coupling, and polydispersity on the statistics of carrier and dispersed phases.

ACKNOWLEDGEMENTS

I would like to offer my gratitude to my research advisor and thesis advisor, Dr. Reetesh Ranjan, for his unwavering support during the completion of this work. It would not have been possible without his consistent guidance along the way. I would also like to extend my gratitude to my thesis committee members, Dr. Kidambi Sreenivas, Dr. Trevor Elliott, and Dr. Abdollah Arabshahi for their continued support during my graduate program at UTC. I want to thank the Fluids and Combustion Modeling Group members, specifically Eli Durant and Robert Smith, for their assistance during the writing of this thesis. A special thank you goes out to the UTC College of Engineering and Computer Science's technical and administrative staff, particularly Ms. Andrea James, for resolving any issues that I faced. I also want to thank the SimCenter administrative staff, specifically Ms. Kim Sapp, for her support with any issues that I faced. I gratefully acknowledge the support of the SimCenter for the Center of Excellence in Applied Computational Science and Engineering (CEACSE) 2020-2021 grant that funded this research, as well as providing the computational resources and technical support to complete this thesis.

TABLE OF CONTENTS

LIST OF FIGURES

LIST OF TABLES

LIST OF ABBREVIATIONS

LDA, Laser-Doppler Anemometer

PIV, Particle Image Velocimetry

CMOS, Complementary Metal Oxide Semiconductor

PDPA, Phase Doppler Particle Analyzer

DNS, Direct Numerical Simulation

LES, Large-Eddy Simulation

RANS, Reynolds-Averaged Navier-Stokes model

FVM, Finite Volume Method

SGS, Subgrid-Scale

KE, Kinetic Energy

PDF, Probability Density Function

EE, Eulerian-Eulerian

EL, Eulerian-Lagrangian

DEVM, Dynamic Eddy Viscosity Model

WALE, Wall-Adapting Local Eddy-viscosity Model

LDKM, Localized Dynamic K-Equation Model

DF, Differential-Filter-Based Dispersion Model

FIT, Fractal Interpolation Technique

KS, Kinematic Simulation

SOI, Spectrally Optimized Interpolation

ADM, Approximate Deconvolution Modeling

TKE, Turbulent Kinetic Energy

LIST OF SYMBOLS

i, Cartesian coordinate directions

x_i, Carrier phase position

$u_{f,i}$, Carrier phase velocity

u_i^+, Carrier phase velocity interpolated at particle position

ρ, Carrier phase density

$x_{\mathrm{p,i}}$, Particulate phase position

$u_{\mathrm{p,i}}$, Particulate phase velocity

ν, Kinematic viscosity

P, Pressure

T, Temperature

τ_{ij}^{sgs}, Subgrid scale viscous stress tensor

$\overline{S}$, Resolved strain-rate tensor

δ_{ij}, Kronecker delta

L, Characteristic length scale

u', Turbulent/subgrid fluctuation velocity component

K_{n}, Knudsen number

λ, Mean free path

N_{p}, Number of particles

V_{p}, Volume of a single particle

V, Volume of computational domain

Φ_{p}, Volume fraction of particles

St, Stokes number

τ_{p}, Particle relaxation time

d, Particle diameter

Ma, Mach number

ν_{t}, Turbulent viscosity

ρ_{p}, Particulate phase density

Δt, Time step size

$\overline{\Delta}$, LES filter size

C_s, Smagorinsky model coefficient

C_k, C_c, σ_k, K-equation model coefficients

τ_{f}, Characteristic time scale of carrier phase

Re_{p}, Particle Reynolds number

b, Model parameter for differential filter model

τ_{w}, Wall shear stress

Re_{H}, Reynolds number based on step height

H, Step height

h, Channel height

U_0, Bulk velocity

$\mathscr{S}$, Traceless symmetric part of the square of the velocity gradient tensor

C_w, WALE model coefficient

σ, Standard deviation of a distribution

Φ_{m}, Mass loading of particles

f, Drag correction factor

x_{R}, Reattachment length

k^{sgs}, Subgrid scale turbulent kinetic energy

CHAPTER 1

INTRODUCTION

Turbulent dispersed multiphase flows, also referred to as particle-laden turbulent flows, commonly occur in many natural and industrial processes, such as aerosolized drug delivery, liquid fuel-based combustion devices, pollutant dispersion in the atmosphere, sedimentation in rivers, etc. [2–6]. Such flows comprise a carrier phase and a dispersed particle phase. Depending upon the mass and volume loading of the dispersed phase, such flows are classified as a dilute suspension, a dense suspension, or a granular flow. The present study focuses on dilute suspensions, where the particle motion dynamics are governed by the carrier phase, but particles may or may not affect the flow dynamics, thus leading to a two-way or a one-way coupling with the flow, respectively. The complex interactions between the phases and the presence of turbulence make the analytical solutions infeasible, thus leading to the study of such flows using experimental and numerical techniques. However, there are challenges to both the strategies when it comes to accurate prediction of statistics of carrier and dispersed phases in practically relevant configurations. Therefore, further improvements in experimental diagnostics and numerical methodologies and models are needed to enable an improved understanding of such flows.

Experimental methods of studying particle-laden turbulent flows can provide more realistic insights into physical processes due to the ability to include the effects of a wide range

of flow conditions and there is no need to perform modeling [7–9]. However, the experiments require more setup and monetary considerations, as well as the entire flow field usually cannot be captured. This is due to only being able to produce finite numbers of measurements, whether in time or space. Optical diagnostic methods also have the limitation of finite speed or resolution, while invasive methods have spatial limitations in order to prevent altering the flow field. Another specific issue associated with particle-laden turbulent flows is the need for tracer particles when utilizing optical methods. These tracer particles are used to represent the carrier or fluid phase but are required to be negligible in size and mass loading compared to the dispersed phase. This implies that obtaining the statistics of both low Stokes numbers (St) and high St granular flows becomes challenging with optical diagnostic techniques.

Numerical methods for the study of particle-laden turbulent flows have contrasting benefits and drawbacks compared to experimental techniques. The benefits of numerical methods are usually lower monetary and setup requirements, being able to run multiple versions of the same case at once, ease of processing results, and resolving the flow field as much as is desired. Drawbacks of numerical methods include modeling of physical phenomena, introducing more numerical dissipation and potential for error, and possibility for non-physical results [10]. In the present work, we focus on low Mach number (Ma) incompressible flows, which makes the computational modeling relatively more simple [11]. A typical approach to simulate such flows is to use the Eulerian-Lagrangian (E-L) framework, which treats the carrier phase as a continuous Eulerian field, and the dispersed phase is viewed with a Lagrangian lens [1, 8]. This method can be used with different approaches,

such as Direct Numerical Simulation (DNS), Reynolds-Averaged Navier-Stokes (RANS), or Large-Eddy Simulation (LES). Each approach has its applications, as DNS is meant for resolving all scales of turbulence everywhere, RANS is meant for steady-state turbulence, as only the mean quantities need to be calculated by modeling turbulence effects, and LES is used for resolving the large scales and modeling the smaller-than-grid scales (subgrid-scale modeling) [12]. The focus of the present study is on the use of LES while employing the E-L framework for the study of two-way coupled particle-laden flows.

Past and current studies have focused on improved modeling strategies for LES of particle-laden turbulent flows [8, 11–14]. However, several challenges need to be addressed to improve the overall predictive capabilities of LES. Beyond the modeling of the carrier phase, which is reasonably well understood, the major challenges are associated with the governing equations describing the evolution of the dispersed phase, coupling of the carrier and the disperse phases, handling of the blockage effects, computational efficiency, and convergence of the solution. Here, we primarily focus on the challenges associated with the coupling aspect of such flows in the context of a LES. Two more particle-dynamic features to consider are the role of polydisperse particle size distribution and turbulence modulation by particles. When polydispersity is taken into account, a more realistic range of inertial effects on the carrier phase can be modeled [15]. It is also important to consider the turbulence modulation by particles, which can be amplified for high Stokes numbers, mass loadings, and particle Reynolds numbers, or attenuated by the converse characteristics [7].

The dispersed phase evolution requires the time history of the carrier phase veloc-

ity. In LES, this is attained using a subgrid turbulence dispersion model. Past studies have used several models, which include stochastic [16–22], deconvolution [11, 23–25], hybrid stochastic/deconvolution [26], and kinematic simulation [27–29] based models. These models approximately reconstruct the subgrid-scale (SGS) fluctuations to enable accurate representation of the instantaneous carrier-phase quantities such as velocity, temperature, etc., at the dispersed phase location. In particular, two-way coupled flows not only represent a larger volume fraction of particles (Φ_p) but include the interactions of particles on the flow. This is where subgrid dispersion modeling is applicable for LES because the motion of particles affects the carrier phase flow field [27]. Another important factor for modeling subgrid dispersion is the Stokes number of the flow because it strongly determines the quality of the results [2]. Some models only work well for low St, while others present the opposite characteristics [27, 30]. The key objective of the research is to assess the accuracy aspects of subgrid models for LES while employing the point-particle-based E-L strategy of two-way coupled particle-laden flows.

To perform the assessment of the subgrid models, the well-established flow configuration referred to as particle-laden turbulent flow over a backward-facing step is considered. The subgrid models are employed for both the carrier and dispersed phases. For the modeling of the SGS stress tensor in the Eulerian simulation of the carrier phase, three closures are considered, which include the dynamic eddy viscosity model (DEVM) [10], the wall-adapting local eddy-viscosity (WALE) model [31], and the locally dynamic SGS kinetic energy model (LDKM) [10]. The dispersion models include stochastic random-walk [19, 32] and the differ-

ential filter [11] models. The results obtained from different modeling strategies are compared with respect to the reference experimental [7] and simulation results [33]. After identifying the best-performing modeling strategy, further studies are carried out to examine the effects of polydispersity and two-way coupling on the statistics of the carrier and the dispersed phases.

1.1 Key Technical Objectives

This thesis aims to contribute to the understanding of the detailed dynamics involved in particle-laden turbulent separating/reattaching flows by meeting the following key technical objectives:

- **Determine the existing subgrid stress model to use for particle-laden simulations:** The most popular turbulence models for LES will be chosen to compare the unladen simulation results to each other and to a posteriori simulation results and experimental results for the same test case. The best-performing model will take into account the computational cost, the speed of implementation, time-averaged and instantaneous features, and most importantly, the agreement with the a posteriori results.

- **Characterize the effects of subgrid dispersion modeling:** Since turbulence displays seemingly random alterations to the flow, the typically coarse grids used in LES require subgrid models to resolve these scales. Particle-laden simulations add another aspect to this problem, in that they require additional dispersion models. The key focus of this study is to further implement and asses subgrid dispersion models for turbulent

particle-laden LES and compare them to experimental and simulation results.

- **Examine the effects of polydispersity and two-way coupling:** The goal is to use the best-performing subgrid models for the SGS stress tensor and dispersion to examine the effects of polydispersity and two-way coupling on the instantaneous and statistical features of carrier and dispersed phases.

- **Investigate the role of Stokes number:** The Stokes number will be varied on the chosen mesh, utilizing the best performing models, by changing the particle diameters. This will lead to variation in the particle response time, which will affect the carrier phase flow in two-way coupled particle-laden flow.

1.2 Thesis Layout

The arrangement of this thesis is broken down as follows. In total, there are seven chapters, including this introductory chapter. Immediately following is a description of how particle-laden turbulent flows are studied in Chapter 2. In Chapter 3, the mathematical formulation of the Eulerian and Lagrangian representations are handled, as well as particle-related parameters and the governing equations for the models. Next, the details of the computational setup and case descriptions are provided in Chapter 4. Then, the computational assessment of subgrid stress modeling, grid convergence, and subgrid dispersion modeling is discussed in Chapter 5. Afterward, the key findings on the effects of inertia, coupling, and polydispersity are covered in Chapter 6. Finally, the major conclusions and future directions of this research are discussed in Chapter 7.

CHAPTER 2

LITERATURE SURVEY

Solid particle transport by a turbulent fluid flow can describe many natural and industrial systems, although the detailed dynamics of such flows, which are marked by complex multi-scale processes and interactions are not completely understood. Another similar class of flows is droplet-laden or bubbly turbulent flows, where the presence of additional physical phenomena such as bubble/droplet deformation, breakup, coalescence, and evaporation leads to increased physical complexities. The applications of such flows are numerous, which include engineering design of several devices, meteorological predictions, sediment transport, pollutant emissions, aerosol deposition, spray combustion, etc. [2–6, 14, 34, 35]. The immense applications of these types of flows have drawn significant interest from researchers in the past. However, further studies are imperative for accurate prediction of physical phenomena prevalent in these flows for newer and improved designs. The literature survey in this chapter focuses on the approaches used to study these flows. The major focus of the survey is on the computational modeling techniques for incompressible particle-laden turbulent flows with particles treated as solid and non-reacting. For a comprehensive survey of particle-laden turbulent flows, the reader is referred to the review articles [1, 8].

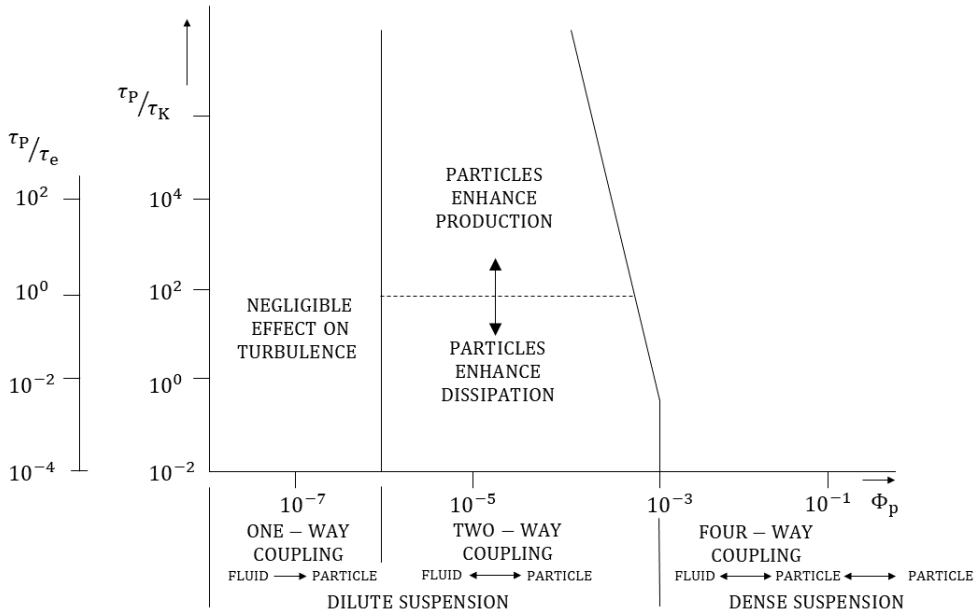

Figure 2.1 Regimes of particle-turbulence interactions, recreated from [1]

2.1 Classification of Particle-Laden Flows

Particle-laden flows are broadly classified into two major regimes, namely, dilute suspension and dense suspension, with further classification into sub-regimes [1, 8]. These regimes are defined based on the volume fraction Φ_p or the mass loading Φ_m of the particles (disperse phase). Here, $\Phi_p = \dfrac{N_p V_p}{V}$, with N_p representing the number of particles, V_p denoting the volume of a single particle, and V representing the total volume occupied by the particles and the fluid. Also, $\Phi_m = \dfrac{N_p V_p \rho_p}{m}$, where ρ_p is the density of a single particle and m is the total mass of fluid. A brief description of these regimes is provided next.

2.1.1 Dilute Suspension

The dilute suspension regime is defined by $\Phi_p \leq 10^{-3}$. It includes two sub-regimes, namely, the one-way coupled regime and the two-way coupled regime. The mass loading is

generally considered to be below 1% for the one-way coupled regime and up to about 100% for two-way coupled regime [8]. Example applications of one-way coupled flows are dispersed micro- and nano-particles used in drug delivery, blood flow, clean-coal gas turbines, and food processing [9, 36]. Fluid-sediment mixtures, pollutants in the atmosphere, and combustion chambers are examples of two-way coupled flows [2–6]

The one-way coupled regime occurs for $\Phi_{\mathrm{p}} \leq 10^{-6}$. In this regime, the particles have a negligible effect on the evolution of the flow field (carrier phase). However, the carrier phase exerts forces on the particles thus affecting the particle dynamics. When the particles concentration is high, i.e., $10^{-6} \leq \Phi_{\mathrm{p}} \leq 10^{-3}$, the flow regime is considered to be two-way coupled. In this sub-regime, the particle dispersion is altered by the carrier phase, and the momentum transfer from the particles affects the evolution of the carrier phase. In the present study, the focus is on dilute suspension with a two-way coupling under turbulent conditions.

2.1.2 Dense Suspension

The second major regime is referred to as dense suspension, which is characterized by $\Phi_p > 10^{-3}$. This regime is also known as the four-way coupled regime, in which particle-particle collisions become important in addition to the two-way coupling between the particles and carrier phase. Applications of this regime include transport of a solid phase by a lubricating fluid, pneumatic transfer of solids in industrial processes, or high-mass loadings of fuel in combustion processes [2, 37].

In the limit when $\Phi_p \to 1$, the flow becomes granular, in which there is no separate

carrier phase. This regime has applications in the transportation of solid particles with a lubricating fluid. Some specific applications of granular flow include the pneumatic transfer of powder in a pipe, reacting or catalyst solid particles/droplets in chemical reactors [6, 38], solid particles in mixed drinks, and sand/other particles in sand storms when dispersed by the turbulent motion of the surrounding air [37].

2.2 Methods of Investigation

Past studies have relied on the extensive use of both experimental and computational techniques to understand the instantaneous and statistical features of two-way coupled particle-laden turbulent flows. While experimental methods provide insight into the actual physical phenomena, they face challenges pertaining to measurements of limited quantities and expenses associated with carrying out such studies. On the other hand, numerical methods can provide detailed insight into such flows over a wide range of conditions, although they face challenges pertaining to the assumptions embedded in the employed mathematical and computational models for such flows. Next, an overview of these approaches and the key challenges faced by them are discussed.

2.2.1 Experimental Methods

Experimental methods for the study of particle-laden turbulent flows are focused on measuring the first and second-order statistics of such flows. These statistics include the mean velocity field and Reynolds stresses of the carrier phase, as well as the mean and fluctuations of the velocity and concentration of the dispersed phase [8]. In addition,

several derived quantities are also of interest, which are usually measured in experimental studies. These include carrier-phase turbulent dissipation rate and dispersed phase velocity correlations. The measurements of dispersed phase statistics are usually carried out using non-invasive photographic techniques, although it is challenging to obtain the statistics of the carrier phase without using tracer particles. Three widely popular techniques include the Laser-Doppler Anemometer (LDA), Particle Image Velocimetry (PIV), and Phase Doppler Particle Analyzer (PDPA). These techniques are briefly discussed next.

The LDA technique has been widely adopted due to the ease of implementation for measuring the statistics of both phases. This system reads the signal of particles based on the light scattering intensity. Therefore, the inertial particles corresponding to the dispersed phase can be differentiated from the lower signals resulting from the tracer particles used for the carrier phase. The differentiation is clarified by signal processing routines searching for specific ranges of the Doppler bursts. The amount of cross-talk from large particles misrepresented as tracer particles is estimated to be less than 5% of the particle-laden flow measurements [7]. At most, this can lead to overestimates of 0.5% for the mean velocity and 20% for the standard deviation of the dispersed phase. Other similar studies that involve LDA for measurements of carrier and dispersed phase velocity components are particle-laden channel flows [39] and coaxial jet nozzles [40].

The PIV method implements light measurements using high-speed CMOS or cross-correlation video cameras and high-repetition-rate lasers to discriminate between the carrier and the dispersed phases [9]. These phases are determined by the cross-correlation of the

short time lag images. A previous version filtered these images by subtracting the tracer-image field from the original image and employing a noise elimination procedure to eliminate the low-intensity halos from the previous tracer particle locations. Many studies have used the PIV method for the unladen backward-facing step flow [41–43] and some have studied the particle-laden case as well [44].

PDPA is another optical method [9], which uses several detectors to measure the phase differences between refractive light measurements, thus providing the particle diameter and velocity measurements. This technique is based on the precision of the angles of the detectors, but can be considered calibration-free and *in situ* traceable, which means it can be related to appropriate standards through an unbroken chain of comparisons. Sudden expansion particle-laden flows have been studied with PDPA [45], which is a larger classification of the backward-facing step flow.

The challenges of using experimental methods for measuring the two-phase flow statistics include the requirement of signal processing and adding tracer particles to represent the carrier phase flow field. These methods face challenges for lower values of Φ_p, and require the concentration of tracers to be much lower than that of the dispersed phase. Even small volume fractions of tracer particles affect the carrier phase flow field, which needs to be taken into account. Measuring the characteristics of non-spherical, non-homogeneously distributed, or opaque particles/bubbles requires adaptation to the current methods. Another challenge is the accumulating error from calculations based on inexact measurements or theory. Higher-order statistics require additional measurements and calculations, which

introduce numerical method error to the experimental error. For example, for continuous profiles of data, the discrete experimental measurement needs to be interpolated with a theoretical curve-fit. To address this particular challenge increased spatial resolution of the experimental measurements is needed.

2.2.2 Computational Methods

The computational techniques for the study of particle-laden turbulent flows corresponding to the dilute suspension regime can be broadly categorized into two types: namely, particle-resolved approach and the point-particle approach [12]. Compared to the particle-resolved strategy, where finite-size particles and the forces resulting from the carrier phase are explicitly accounted for, in the point-particle strategy, the size of the particles and resulting forces from the carrier phase are accounted for implicitly through employing phenomenological models for the forces. The particle-resolved strategy is typically used for assessing and improving the phenomenological models employed by the point-particle approach, as it can only be used to simulate fewer particles. The point-particle approach, which is considered in this study, is applicable when the size of particles is smaller than the resolved scales of the flow field.

Within the point-particle approach, there are two well-established techniques for the simulation of particle-laden flows. These include the Eulerian-Lagrangian (EL) and the Eulerian-Eulerian (EE) frameworks [1, 8, 12]. In both these frameworks, the carrier phase is simulated using an Eulerian formulation. However, the dispersed phase evolution is handled differently in the EE and EL approaches. In the EE framework, the dispersed phase is

considered a continuum, and transport equations for the dispersed phase are solved in an Eulerian manner. On the other hand, in the EL framework, the dispersed phase is treated as a particle or parcel and its dynamics are evolved in a Lagrangian manner.

The EE framework is typically effective for the cases with a very high particle loading, which implies a near-zero Knudsen number [35]. The Knudsen number, (K_n), is described by $K_n = \frac{\lambda}{L}$, where λ is the mean free path, and L is the characteristic length scale. The scenario of a very small value of K_n implies that the distribution of the velocity of the dispersed phase is nearly Maxwellian. This leads to spontaneous clusters of the dispersed phase, which are not representative of the actual physical phenomena. In addition, there are other challenges with the EE framework, which include a higher computational cost while dealing with polydispersity and collision of particles and the inability to accurately account for particle trajectory crossing phenomenon. These challenges, particularly accounting for different types of physical phenomena associated with the dispersed phase are easier to handle within the EL framework, which is employed in this study. Some challenges associated with the EL framework include inefficient parallel scalability of the algorithm when particles are not distributed evenly within the computational domain, numerical instabilities, particularly in two-way coupled flows, and lack of convergence of dispersed phase statistics particularly in the cases exhibiting preferential accumulation of particles.

As mentioned before, within both EE and EL frameworks, the carrier phase flow is simulated using an Eulerian formulation, where the governing equations can be solved using different numerical approaches with varying levels of fidelity and computational costs.

These approaches include direct numerical simulation (DNS), large-eddy simulation (LES), and Reynolds averaged Navier-Stokes (RANS). In DNS, all the spatial and temporal scales are resolved, making it computationally expensive. Therefore, DNS is typically used for the fundamental investigation of flows in canonical to moderately complex configurations at low to moderately high Reynolds number (Re). In LES, only the large-scale flow features are explicitly resolved, and the effects of the unresolved small-scale features of the flow field, also referred to as subgrid-scale (SGS) features, on the resolved flow field are parametrized by using SGS closures. In RANS, all the turbulent fluctuations effects are modeled, making it the least expensive computational modeling strategy. Past studies have shown the superiority of the LES strategy over RANS in flows where the role of unsteady aspects of the flow field are important. Therefore, LES is considered in this study. However, LES on its own suffers from several challenges, which include robust and accurate SGS models for a wide range of flow conditions for both the carrier and dispersed phases, higher computational cost in capturing the near-wall dynamics in wall-bounded turbulent flows, difficulties in modeling of the laminar-to-turbulent transition, and grid convergence. Therefore, further studies are needed to assess and improve the predictive capabilities of the LES strategy while using the EL framework. Further details related to LES-based studies of particle-laden turbulent flows are discussed next.

2.3 Large-Eddy Simulation Strategy

LES is a promising approach for simulation of high Re turbulent flows in practically relevant configurations [26, 46]. This is because LES only resolves the large eddies by using

coarser computational meshes, thus making it computationally efficient compared to DNS. It explicitly solves for the low pass filtered flow field and models the effects of the unresolved small-scales of motion on the resolved large-scales of motion through the use of SGS closures. While simulating particle-laden flows using the EL framework, LES can handle mono-disperse or poly-disperse particle distributions using either the point-particle method or the particle-resolved method [8].

To perform LES of incompressible particle-laden turbulent flows: two types of SGS closures are required to account for the effects of unresolved scales of motion. The first SGS closure is used to model the SGS stress tensor in the momentum equation for the carrier phase, and the second closure is needed to account for the SGS effects on the particle dynamics, also known as subgrid dispersion [27]. These are sometimes referred to as fluid-LES and particle-LES models, respectively. As the computational mesh employed by LES is coarse in comparison to DNS, the use of robust, accurate, and efficient subgrid models is key for accurate predictions. This is especially true for wall-bounded turbulent flows, which is the focus of the present study.

In such flows, the near-wall dynamics exhibit features such as subgrid anisotropy and nonequilibrium behavior, which need to be accounted for in the employed SGS closures. The challenges for LES are increased in particle-laden turbulent flows from the subgrid modeling perspective as in such flows, a subgrid model is needed for the dispersion of the particles, which is highly dependent on the inertia of the particles. These challenges faced by the subgrid models have led to extensive research in the past, on the development of newer and

improved SGS models for LES of particle-laden turbulent flows. Next, a brief description of these SGS closures is presented.

2.3.1 Modeling of Subgrid Stress Tensor

The governing equations for the LES of incompressible turbulent flow comprise the spatially filtered equations for the conservation of mass and momentum. The assumption of incompressible flow is usually valid for low Mach number (Ma) flows, i.e., $Ma \lessapprox 0.3$. Here, Ma is defined as the ratio of characteristic velocity scale to the speed of sound. The spatial filtering of the momentum balance equation leads to the appearance of terms, which require further closure models. Essentially, the nonlinear advection term, when filtered, leads to the well-known closure problem in the form of the SGS stress tensor (τ_{ij}^{sgs}) term, which is represented by $\tau_{ij}^{\text{sgs}} = \overline{u_i u_j} - \overline{u}_i \overline{u}_j$. Note that in LES, governing equations are solved to obtain $\overline{u}_i$, and therefore, the nonlinear filtered term $\overline{u_i u_j}$ remains unknown. A wide range of closure models is available in the literature for the modeling of τ_{ij}^{sgs} [47]. All of the modeling approaches have their strengths and limitations when it comes to simulating flows in different configurations. For predictive simulations using LES as a tool, the SGS model for τ_{ij}^{sgs} should be robust, accurate, and efficient.

For single-phase turbulent flows, some of the most commonly used SGS models include the algebraic (Smagorinsky) eddy viscosity model [48], the one-equation model for the subgrid kinetic energy [49], and dynamic models [49, 50]. These models have been used successfully in the past to study a wide range of turbulent flows. However, LES of high Re complex wall-bounded turbulent flows is still subject to several challenges that remain un-

resolved. Some of these challenges are a realistic representation of the subgrid stress tensor [46], commutation errors due to the non-uniform grid used for complex flows [51], ability to accurately resolve the dynamically dominant near-wall structures [52], modeling laminar-to-turbulent transition, and the transition between near-wall and far-field free shear flows without requiring *ad hoc* fixes.

LES-based studies of particle-laden turbulent flows have usually employed the SGS closures developed for the single-phase turbulent flows. Therefore, in the present study, both algebraic and one-equation-based models have been considered to examine their performance. These models are briefly discussed next.

The first class of models for the SGS stress tensor is referred to as algebraic models. A common way to attain closure of the SGS stress tensor is to assume the form given by

$$\tau_{ij}^{\text{sgs}} - \frac{\tau_{kk}^{\text{sgs}}}{3}\delta_{ij} = -2\nu_t \overline{S}_{ij}, \tag{2.3.1}$$

where ν_t is the unknown eddy viscosity and $\overline{S}_{ij}$ is the resolved strain rate given by

$$\overline{S}_{ij} = \frac{1}{2}\left(\frac{\partial \overline{u}_i}{\partial x_j} + \frac{\partial \overline{u}_j}{\partial x_i}\right). \tag{2.3.2}$$

A classical method to obtain eddy viscosity is due to Smagorinsky [48] that relates the eddy viscosity to the resolved strain rate tensor and grid resolution through $\nu_t = C_s \overline{\Delta}^2 |S|$, where $|S| = 2(\overline{S}_{ij}\overline{S}_{ij})^{1/2}$, $\overline{\Delta}$ is the LES filter size, and C_s is the Smagorinsky coefficient. In isotropic turbulent flows, $C_s = 0.16$ is obtained based on equilibrium assumption where energy transfer

is equal to the viscous dissipation [53]. However, for other types of flows, for example, wall-bounded, shear, or transitional flows, this value of C_s produces higher dissipation. In these cases, the value of C_s can be obtained using a dynamic approach [50]. The dynamic version of the Smagorinsky model is referred to as the dynamic eddy viscosity model (DEVM). It uses a test filter, usually around $2\overline{\Delta}$, and solves for the coefficient C_s. To capture the near-wall dynamics, the well-known van Driest damping is used near the walls, although the asymptotic behavior of the near-wall eddy viscosity is not captured with such an approach [31]. To address this, the wall-adapting local eddy-viscosity (WALE) model [31] can be used, which is another type of algebraic model. It recovers the proper scaling of ν_t in the near-wall region, and therefore, eliminates the need for damping functions or dynamic procedures. Additionally, only local information is needed to build the eddy viscosity field. Furthermore, the model has also shown abilities to handle the transition to turbulence behavior without requiring any further adjustments.

Another classification of the SGS stress tensor models is equation-based methods [49, 54–56]. One of the most frequently used models is the one-equation based model, where the eddy viscosity is given by $\nu_t = C_\nu \sqrt{k^{\text{sgs}}}\overline{\Delta}$. Here k^{sgs} is the subgrid-scale turbulent kinetic energy

$$k^{\text{sgs}} = \frac{1}{2}\left(\overline{u_k u_k} - \overline{u}_k \overline{u}_k\right), \tag{2.3.3}$$

which is determined by solving a modeled transport equation for k^{sgs}. This modeling approach shows a weak dependence on the filter size and Re, which indicates that LES with

this model can be used for a wide range of high Re flows utilizing coarse computational grids. It has also shown a good correlation with the DNS results for the production and transport terms in the *a priori* assessment studies. However, the static formulation of this model faces problems related to the dissipation terms, which is addressed by the dynamic version of this model, referred to as the locally dynamic subgrid kinetic energy model (LDKM) [49, 56]. A similarity assumption is invoked by the LDKM to the dissipation term in the subgrid kinetic energy transport equation. Additionally, LDKM does not make the same local equilibrium assumption as the DEVM. However, compared to the static one-equation-based model, the LDKM introduces further computational procedures. As both static and dynamic models require to solve an additional transport equation to determine k^{sgs}, they tend to be computationally expensive compared to the class of algebraic models.

There are other SGS stress models for specific classes of flows, as well as many improvements to the existing models. These include stochastic back-scatter [57, 58], scale similarity [59, 60], and Fourier-space-based [61] subgrid models to name a few. However, as noted before, all the modeling approaches still face challenges particularly when it comes to the investigation of different types of flow conditions. The challenges are increased further for the simulation of particle-laden flows due to the added complexity of coupling effects between the carrier and the dispersed phases. In the present study, therefore, we have considered the models which have shown promising results for different types of single-phase turbulent flows. Specifically, DEVM, WALE, and LDKM have been considered in this study. Some preliminary studies based on Smagorinsky's model and the constant-coefficient based one-

equation model yielded higher levels of differences with the reference experimental results, and therefore are not considered further.

2.3.2 Subgrid Dispersion Modeling

The coupling in the EL framework corresponds to the effects of the carrier phase on the dispersed phase and *vice-versa*. For example, the dispersed phase evolution requires the time history of the carrier phase velocity at the location of the particles (u_i^+). While performing a DNS, u_i^+ can be obtained by interpolating the carrier phase velocity field (u_i) at the particle location. However, in LES, the carrier phase velocity field is decomposed into its resolved and subgrid constituents by employing a spatial filter through $u_i = \overline{u}_i + u_i'$, and only the resolved velocity field is explicitly solved. Here $\overline{u}_i$ is the resolved velocity and u_i' is the subgrid velocity component. As the subgrid velocity is not explicitly known, therefore, to get u_i^+, an approximation is needed, which is referred to as subgrid dispersion modeling. Past studies have used several models, which include stochastic [16–22], deconvolution [11, 23–25], hybrid stochastic/deconvolution [26], and kinematic simulation [27–29] based models. These models approximately reconstruct the subgrid-scale (SGS) fluctuations to enable accurate representation of the instantaneous carrier-phase velocity, at the dispersed phase location.

Note that the amount of energy that the subgrid scales provide is defined by the physical parameters, which include the mass loading of particles, particle injection speed, distribution of particle sizes, and other relevant non-dimensional parameters. The two key non-dimensional parameters that characterize the subgrid dispersion effects include, the particle Reynolds number based on the slip velocity and particle diameter (Re_p =

$|(u_{p,i} - u_i)(u_{p,i} - u_i)|^{1/2} (d/2\nu))$ and the Stokes number ($St = \tau_p/\tau_f$) [2, 12, 62]. Here, τ_p and τ_f denote the characteristic time scales for the dispersed and the carrier phases, and ν is the kinematic viscosity of the dispersed phase. For small St, the particles are inertial with respect to subgrid eddies, and on the opposite limit, they are ballistic with respect to the eddies [63]. The first regime is where the particles become more fluid-like and increase the turbulence spectral density. The latter is where they are less responsive to the flow field, act as random walkers, and attenuate the turbulence spectral density. In both limits, as St approaches 0 and ∞, the particles become more uniformly distributed. In the intermediate region, i.e., $St \sim \mathcal{O}(1)$, the particles respond to vortical and straining features of the local carrier phase flow field leading to non-uniform distribution of particles.

Due to different types of dynamics exhibited by particle-laden turbulent flows dependent upon Re_p and St, the subgrid dispersion models proposed so far in the literature tend to perform better for certain types of conditions to capture the features such as dispersion, energy transfer, preferential concentration, and other metrics [11, 26, 62]. As a key focus of the present study is to evaluate the performance of the established subgrid dispersion models, we briefly describe some of the commonly used models, which include a no model approach, stochastic approach, spectral technique, kinetic simulation model, and fractal model.

In the no-model approach, $u_i^+ = \overline{u}_i$ is used, which implies using the filtered carrier-phase velocity field at the dispersed phase location, thus neglecting the subgrid dispersion completely. In the stochastic approaches, $u_i^+ = \overline{u}_i + u_i'$ is used, where u_i' is obtained through stochastic approaches such as the random walk (RW) or the Langevin equation-based modes.

The stochastic model relying on the Langevin type equation to obtain u_i'' uses a random source in the particle equation of motion. The equation originally was developed for the particle subgrid turbulent velocity and was extended later to model the carrier phase velocity field seen by the inertial particles [12, 32]. Such an approach provides the high-frequency forces exerted by the unresolved eddies on the particle motion. An alternate approach to obtain u_i' is to use the approximate deconvolution (AD) model, which tends to yield better results in high St flows [21]. For example, it has shown improved prediction of particle turbulent kinetic energy, turbulence diffusivity, and preferential concentration compared to the other modeling approaches, particularly for homogenous shear flows. A specific example of this class of models, which is considered in this study is the differential filter (DF) based model, which relies on the use of elliptic differential filters [11].

Both stochastic and AD types of subgrid dispersion models have challenges in representing a broad range of scales. For example, the Langevin equation-based model miscalculates the preferential concentration due to being dispersive for all values of St [11]. Therefore, the approach does not work well at higher Stokes numbers because it does not account for the crossing trajectory effect of the particles [21]. Furthermore, for $St \sim \mathcal{O}(1)$ the probability density function (PDF) of particle acceleration has shown wider tails than those reported by DNS studies [30]. On the other hand, in the AD-based model, only the largest of the unresolved scales are captured due to multiple implicit filtering operations, therefore it is not well-suited for low St flows. The DF dispersion model has not been tested for the two-way or four-way coupled regimes in the past, and therefore, needs further studies.

A hybrid stochastic-deconvolution model has shown improved predictions in particle-laden turbulent channel flows, which is independent of Re and St [12]. However, further studies are needed to examine the capabilities of such an approach for different flow regimes and to different flow configurations.

Another class of models is synthetic field models, which create a synthetic field to capture the essential features of the subgrid scales [64]. These methods are based on the physical assumptions of the small eddies' energy content. A particular approach is the fractal interpolation technique (FIT), which maps the large-scale eddies to increasingly smaller scales [13, 64]. The model can handle the energy dissipation to take place and backscatter to occur. It performs well for predicting particle velocity and concentration statistics in the flow regions where the turbulence is close to being homogeneous and isotropic. The challenges are in estimating the stretching parameters needed by the model for non-homogeneous flows. In addition, the model does not always provide a correct reconstruction of the correlation of different velocity components.

A less frequently used model is the kinematic simulation model, which aims at spectrally regenerating the unresolved scales of turbulence by incorporating high wavenumber modes in the velocity field [11, 13, 65]. It requires a known turbulent kinetic energy spectrum to produce the subgrid velocity field. For homogeneous isotropic flows, this method performs well and is computationally inexpensive, but involves non-trivial solutions in wall-bounded flows. Furthermore, this is a computationally expensive method, although it is promising for predicting preferential concentration and velocity statistics at higher Stokes numbers.

Spectrally optimized interpolation (SOI) is another less commonly used model, which uses an interpolation stencil that requires multiple pre-processing steps in order to interpolate the fluid velocity seen by the particles [27]. SOI is known to work well for predicting the kinetic energy of particles at higher Re, which includes the inertial range. This method provides good agreement with DNS results of preferential concentration and clustering metrics for $St \geq 1$, yet it over-predicts the preferential concentration at $St < 1$.

It is evident that further studies are needed to improve upon the existing models, which either works for canonical configurations or for certain ranges of St. Furthermore, more studies are needed to assess the performance of the existing models for the LES of two-way coupled particle-laden turbulent flows, so that the challenges with the existing approaches can be identified. In the present study, the performance of the no-model, the RW-based stochastic model, and the DF dispersion model is assessed in comparison to the reference experimental results.

2.4 Summary

Particle-laden turbulent flows have been extensively studied in the past using experimental and computational techniques due to the immense applications of such flows. However, both approaches face challenges for accurate predictions of statistics of the carrier and the dispersed phases. Specifically, the experimental techniques relying on optical diagnostics employing tracer particles suffer from the challenge to differentiate between the tracer and inertial particles and often tend to be limited to measurements of fewer quantities or at certain operating conditions. On the other hand, numerical approaches suffer

from the challenges related to the employed mathematical and computational models for the simulation of such flows.

In this study, the well-established Eulerian-Lagrangian framework is used to perform LES of two-way coupled particle-laden turbulent flows. For the carrier phase, compared to DNS where all the relevant scales are resolved, and RANS where turbulence is modeled completely, LES solves for large scales and parametrizes the effects of small scales in the form of the SGS closure models. Therefore, LES tends to be a promising approach for computationally tractable and accurate simulations of flows observed in practically relevant configurations and conditions. However, robust, accurate, and efficient SGS closures are needed to ensure LES with predictive capabilities. In the EL framework, the dispersed phase is tracked in a Lagrangian manner, which again requires a closure approximation for the subgrid fluctuation of the carrier phase velocity seen by the dispersed phase while performing LES. This is accomplished by the use of subgrid dispersion models.

A wide range of SGS closures are available to model the subgrid effects in the governing equations for the carrier and the dispersed phase. However, they face several challenges for simulation of particle-laden turbulent flows, which are related to an accurate description of the subgrid effects for different values of Re, Re_{p} and St and in different flow configurations. Therefore, further studies are needed to examine the capabilities of the currently available models. This is particularly more relevant for the two-way coupled particle-laden turbulent flows, which is the focus of this study.

CHAPTER 3

MATHEMATICAL FORMULATION AND NUMERICAL METHODOLOGY

In this chapter, the governing equations for LES of the two-way coupled particle-laden turbulent flow are discussed first, along with a description of the subgrid models. Afterward, a description of the numerical methodology is provided. As stated before, the Eulerian-Lagrangian formulation is considered for LES in this study, where the equations of the carrier phase are described by the filtered Navier-Stokes equations, and the dispersed particles are tracked in a Lagrangian manner. Furthermore, incompressible flow formulation is considered with the assumption that the fluid behaves as a Newtonian fluid. The particles are considered perfect spheres with constant diameter and constant temperature.

3.1 Governing Equations

For flows below Mach number of 0.3, the governing equations can be simplified due to the incompressible flow assumption, therefore compressibility effects are neglected. The incompressible Navier-Stokes equations for LES of the carrier phase are obtained by spatially filtering the Navier-Stokes equations using a convolution kernel [12, 66]. For example, spatial filtering of a field variable $\phi(\boldsymbol{x}, t)$ is performed by convolution of $\phi(\boldsymbol{x}, t)$ with a filter kernel

$G(\boldsymbol{x}, \boldsymbol{x}'; \overline{\Delta})$ through

$$\overline{\phi}(\boldsymbol{x}, t) = \int_{\Omega} \phi(\boldsymbol{x}', t)\ G(\boldsymbol{x}, \boldsymbol{x}'; \overline{\Delta})\ d\boldsymbol{x}', \tag{3.1.1}$$

where $\overline{\phi}(\boldsymbol{x}, t)$ is the filtered or the resolved field and $\overline{\Delta}$ is the filter width. The spatial filtering operator is essentially a low-pass filter where higher wavenumber contributions are filtered out. The filter kernel $G(\boldsymbol{x}, \boldsymbol{x}'; \overline{\Delta})$, is in general, a weighting function with a support, which vary depending upon the filter type and the filter width. In this study, we consider the filter kernel to be a top-hat filter expressed as

$$G(\boldsymbol{x}, \boldsymbol{x}'; \overline{\Delta}) \equiv G(\boldsymbol{x} - \boldsymbol{x}'; \overline{\Delta}) = \begin{cases} 1 & \text{if} \quad |\boldsymbol{x} - \boldsymbol{x}'| \leq \dfrac{\overline{\Delta}}{2}, \\ 0 & \text{otherwise,} \end{cases} \tag{3.1.2}$$

which corresponds to a local volume-averaging and has a global support in the spectral space contrary to the spectral cut-off filter. Additionally, we consider an implicit LES where the employed computational grid acts as the filter and therefore, no explicit filtering is performed. The spatial filtering operation, when applied to turbulent velocity field u_i, separates the velocity field into an energy containing resolved component and a dissipation containing SGS component. The subgrid-scale component u_i' also contains the unresolved energy and is defined from the Leonard decomposition as

$$u_i'(\boldsymbol{x}, t) = u_i(\boldsymbol{x}, t) - \overline{u}_i(\boldsymbol{x}, t), \tag{3.1.3}$$

which differs from the Reynolds decomposition as the filtered value of the subgrid-scale is not zero, i.e., $\overline{u_i'} \neq 0$ and the filtered field is not idempotent, i.e., $\overline{\overline{u}}_i \neq \overline{u}_i$.

Applying the filtering operation to the incompressible Navier-Stokes and continuity equations leads to the well known LES equations

$$\frac{\partial \overline{u}_i}{\partial x_i} = 0, \tag{3.1.4}$$

$$\frac{\partial \overline{u}_i}{\partial t} + \frac{\partial \overline{u}_i \overline{u}_j}{\partial x_j} = -\frac{\partial \overline{p}}{\partial x_j} + \nu \frac{\partial^2 \overline{u}_i}{\partial x_j \partial x_j} - \frac{\partial \tau_{ij}^{\text{sgs}}}{\partial x_i} + \overline{\mathcal{F}}_i + \overline{\mathcal{S}}_i, \tag{3.1.5}$$

where $\overline{u}_i$ is the filtered velocity, $\overline{p}$ is the filtered pressure, τ_{ij}^{sgs} is the SGS stress tensor, $\overline{\mathcal{F}}_i$ denotes the filtered body-force term per unit mass, and $\overline{\mathcal{S}}_i$ denotes the forcing term per unit mass resultant from the dispersed phase. The SGS stress term represents the effect of subgrid fluctuations. It is given by

$$\tau_{ij}^{\text{sgs}} = \overline{u_i u_j} - \overline{u}_i \overline{u}_j, \tag{3.1.6}$$

and requires further modeling to close the governing LES equations for the carrier phase.

While using the E-L framework, particles are tracked in a Lagrangian manner. The particle trajectory equation with the point-particle assumption is given by

$$\frac{dx_{\text{p},i}}{dt} = u_{\text{p},i}, \tag{3.1.7}$$

where, $x_{\text{p},i}$ is the particle position, and $u_{\text{p},i}$ is the particle velocity in Cartesian coordinates.

The equation of motion is given as

$$\frac{du_{\mathrm{p},i}}{dt} = \frac{f(Re_{\mathrm{p}})}{\tau_{\mathrm{p}}}\left(u_i^+ - u_{\mathrm{p},i}\right) - g\left(1 - \frac{\rho}{\rho_{\mathrm{p}}}\right)\delta_{i2}, \tag{3.1.8}$$

where, u_i^+ is the carrier phase velocity interpolated at the particle position, $f(Re_{\mathrm{p}})$ is the drag factor, g is the magnitude of the acceleration due to gravity, ρ is the carrier phase density, ρ_{p} is the density of the particle, and τ_{p} denotes the particle response time given by

$$\tau_{\mathrm{p}} = \frac{d^2}{18\nu}\frac{\rho_{\mathrm{p}}}{\rho}, \tag{3.1.9}$$

with d denoting the diameter of the particle.

The drag factor f is an empirical correlation used to modify the Stokes drag for large Re_{p} with Re_{p} being the particle Reynolds number, which is given by

$$Re_p = \frac{\rho_p d\left|u_i^+ - u_{\mathrm{p},i}\right|}{\rho\nu}. \tag{3.1.10}$$

The empirical correlation $f(Re_{\mathrm{p}})$ is given by [67]

$$f(Re_{\mathrm{p}}) = \begin{cases} 1 + \dfrac{1}{6}Re_{\mathrm{p}}^{\frac{2}{3}}, & Re_{\mathrm{p}} \leq 1000 \\ 0.424\dfrac{Re_{\mathrm{p}}}{24}, & Re_{\mathrm{p}} \geq 1000 \end{cases}. \tag{3.1.11}$$

In this study, it is assumed that the particle radius is smaller than the smallest carrier phase length scale that is resolved, and the particle density (ρ_{p}) is much greater than the density

of the carrier fluid (ρ). Many other particle forces have not been considered, such as the Magnus force, Saffman lift force, and buoyancy, due to the assumed ratio of particle density to fluid density being greater than 1000 [8, 33, 68]. This is not true for every particle-laden flow, but for this study, the preceding equations apply.

3.2 Subgrid Modeling

As discussed in Chapter 2 and Sec. 3.1, LES of particle-laden turbulent flows using the E-L framework requires closure models for the SGS stress tensor term in the carrier phase momentum equation and the subgrid dispersion term in the Lagrangian evolution equation for the dispersed phase. In this study, four different types of closures for the SGS stress are considered. These include a no-model strategy, the dynamic eddy viscosity model (DEVM) [50], the WALE model [31], and the one-equation based locally dynamic kinetic energy model (LDKM). For the subgrid dispersion, three models are considered, which include the no-model strategy, the stochastic random-walk (RW) model, and the differential filter (DF) based model. A brief description of these models is provided next.

3.2.1 Models for SGS Stress Tensor

All the three closures for the SGS stress tensor considered in this study rely on the eddy viscosity (ν_t) based approach for a closure of the SGS stress tensor through:

$$\tau_{ij}^{\text{sgs}} - \frac{\tau_{kk}^{\text{sgs}}}{3}\delta_{ij} = -2\nu_t \overline{S}_{ij}, \tag{3.2.1}$$

where $\overline{S}_{ij} = \frac{1}{2}\left(\frac{\partial \overline{u}_i}{\partial x_j} + \frac{\partial \overline{u}_j}{\partial x_i}\right)$ is the resolved strain-rate tensor. While DEVM and WALE are are algebraic closures, the LDKM is a one-equation based closure. The three models considered here differs in the way ν_t is obtained.

In the DEVM, ν_t is given by

$$\nu_t = C_s \overline{\Delta}^2 |S|, \text{ where } |S| = \sqrt{2\overline{S}_{ij}\overline{S}_{ij}}. \tag{3.2.2}$$

Here, C_s is the Smagorinsky coefficient. Compared to the Smagorinsky model where C_s is specified to be constant, DEVM computes C_s in a dynamic manner proposed by Germano et al. [50], Lilly [69]. The dynamic procedure uses a test filter, typically of size $\backsim 2\overline{\Delta}$, to determine the model coefficient C_s through

$$C_s = -\frac{1}{2}\frac{\langle L_{ij} M_{ij} \rangle}{\langle M_{kl} M_{kl} \rangle}. \tag{3.2.3}$$

Here, $\langle \cdot \rangle$ denotes a local averaging procedure over the faces of a finite volume cell, and the test filtering operation is denoted by $\widehat{(\cdot)}$. In above equations, L_{ij} and M_{ij} are respectively, given by

$$L_{ij} = \widehat{\overline{u_i}\overline{u_j}} - \widehat{\overline{u}_i}\widehat{\overline{u}_j}, \tag{3.2.4}$$

$$M_{ij} = \widehat{\Delta}^2 |\widehat{\overline{S}}| \widehat{\overline{S}_{ij}} - \overline{\Delta}^2 \widehat{|\overline{S}| \overline{S}_{ij}}. \tag{3.2.5}$$

The algebraic WALE model [31] can be used without wall functions or global damping

functions while simulating wall-bounded turbulent flows. As it belongs to the algebraic class of models, it leads to an efficient approach to obtain the eddy viscosity. Furthermore, compared to DEVM no test filtering and the dynamic procedure are needed in this approach. In addition, the model accounts for the effects of both the strain and the rotation rate of the smallest resolved turbulent fluctuations and can recover the appropriate scaling of the eddy viscosity in the near-wall region. The eddy viscosity in the WALE model is expressed as:

$$\nu_t = \left(C_w \Delta^2\right) \frac{\left(\mathscr{S}_{ij}^d \mathscr{S}_{ij}^d\right)^{3/2}}{\left(\bar{S}_{ij}\bar{S}_{ij}\right)^{5/2} + \left(\mathscr{S}_{ij}^d \mathscr{S}_{ij}^d\right)^{5/4}}, \tag{3.2.6}$$

where, $\mathscr{S}_{ij}^d = \frac{1}{2}\left(\bar{g}_{ij}^2 + \bar{g}_{ji}^2\right) - \frac{1}{3}\delta_{ij}\bar{g}_{kk}^2$ is the traceless symmetric part of the square of the velocity gradient tensor $\bar{g}_{ij} = \partial\overline{u_i}/\partial x_j$, and C_w is a model constant. In the present study, $C_w = 0.325$ has been used.

An alternate approach to obtain ν_t is to relate it to the SGS turbulent kinetic energy k^{sgs} through [54]

$$\nu_t = C_\nu \overline{\Delta} \sqrt{k^{\text{sgs}}}, \tag{3.2.7}$$

where $k^{\text{sgs}} = \frac{1}{2}\left(\overline{u_k u_k} - \overline{u}_k \overline{u}_k\right) = \frac{\tau_{kk}^{\text{sgs}}}{2}$. An additional modeled transport equation is solved to determine k^{sgs} [54], and the coefficient C_ν is determined locally (both in space and time) in a dynamic manner using LDKM [49, 56]. The modeled transport equation for k^{sgs} is given

by

$$\frac{\partial k^{\text{sgs}}}{\partial t} + \frac{\partial}{\partial x_j}\left(\overline{u}_j k^{\text{sgs}}\right) = -\tau_{ij}^{\text{sgs}}\overline{S}_{ij} + \frac{\partial}{\partial x_j}\left[\left(\nu + \nu_t\right)\frac{\partial k^{\text{sgs}}}{\partial x_j}\right] - C_\epsilon \frac{\left(k^{\text{sgs}}\right)^{3/2}}{\overline{\Delta}}. \tag{3.2.8}$$

In the right-hand side of the above equation, the three terms denote production, molecular and turbulent diffusion, and dissipation of k^{sgs}, respectively. Furthermore, C_ϵ is another model coefficient, which is also determined dynamically in a similar manner to the other model coefficient C_ν [49]. To determine the two model coefficients, test filter fields are used, where the test filter ($\widehat{\Delta}$) is consistent with the grid filter ($\overline{\Delta}$). It is prescribed as $\widehat{\Delta} = 2\overline{\Delta}$. For further details of the dynamic procedure employed in the LDKM, the reader is referred to the cited references.

Note that the LDKM formulation is well-posed and does not require algorithmic adjustments such as spatial averaging along homogeneous directions [56]. In terms of the computational cost, the LDKM formulation has an extra cost compared to the algebraic approaches DEVM and WALE model considered here, as it requires the solution of the transport equation for k^{sgs}. However, it has the advantage over the algebraic approach as the equilibrium assumption is not required. Finally, k^{sgs} provides a more accurate estimate for the SGS velocity scale, which can be used for problems related to turbulence interaction with other transport processes such as heat transfer, mass transfer, combustion, etc., and modeling of the subgrid dispersion.

3.3 Subgrid Dispersion

The coupling between the carrier and the dispersed phase occurs through u_i^+ in the governing equation for the particle velocity (see Eq. (3.1.8)). Here, u_i^+ denotes the velocity of the carrier phase at the particle location. In a direct numerical simulation, it is obtained by interpolating instantaneous velocity u_i from the computational grid to the location of the particle. However, in LES, the solution for the resolved velocity field $\overline{u}_i$ is computed. Therefore, the resolved turbulent kinetic energy that is captured in LES misses the subgrid contributions, which is typically around 15-20% of the total turbulent kinetic energy [21]. The amount of subgrid contributions is dependent upon the grid resolution, the turbulent intensity, the inertia of particles, and other factors such as near-wall effects. It is apparent that such an amount of subgrid contribution can play a role in the dynamics of the dispersed phase. This is addressed by the use of subgrid dispersion models [13] to get an approximate representation of u_i^+. In the present study, three approaches are considered, which include the no-model approach, the random walk (RW) model, and the differential filter (DF) based model.

In the no-model strategy, the effects of subgrid dispersion is completely neglected. Therefore, the approximation of u_i^+ is given by

$$u_i^+ = \overline{u}_i. \tag{3.3.1}$$

Such an approach in an LES can lead to inaccuracies in the prediction of particle dynamics, particularly when the SGS kinetic energy is significant or the particle time constant is small

[70]. Both these conditions are prevalent in LES of practically relevant flows where usually coarse grids are used for computational efficiency.

The stochastic RW subgrid dispersion model assumes the subgrid turbulence to be isotropic and have a Gaussian probability distribution [16]. The approximation for u_i^+ in the RW model is specified through [71]

$$u_i^+ = \overline{u}_i + X\sqrt{\frac{2}{3}k^{\text{sgs}}}, \tag{3.3.2}$$

where X is a random number based on the normal distribution with zero mean and unit variance.

The DF based subgrid dispersion model [11] belongs to the class of approximate deconvolution method, which attempts to perform a reversal of the LES filtering, to capture the energy associated with the barely resolved scales [27]. In this model, the approximation for u_i^+ is given by

$$u_i^+ = \overline{u}_i - \frac{\partial}{\partial x_j}\left(b^2\frac{\partial \overline{u}_i}{\partial x_j}\right). \tag{3.3.3}$$

Here, b is a model parameter, which is chosen to be the LES filter width, i.e., $b = \overline{\Delta}$. The model parameter can be determined dynamically, which can be considered in a future study.

3.4 Numerical Methodology

The computational studies are performed using UTCFOAM, which is an in-house extended version of the OpenFOAM software framework [72]. In the UTCFOAM, several

of the subgrid dispersion models have been implemented, which are not part of the base OpenFOAM software. This includes the DEVM for the SGS stress tensor and the subgrid dispersion models for LES [73]. The details of the numerical methods employed by the solvers for the carrier and dispersed phases are briefly discussed next.

3.4.1 Carrier Phase Solver

The governing equations for the carrier phase given by Eq. (3.1.4) and Eq. (3.1.5) are spatially discretized using the finite volume method (FVM). The use of FVM allows for an easier formulation using an unstructured computational mesh, which is useful for simulation of complex configurations. Additionally, it can discretely ensure all the conservation laws. The computational mesh considered in this study is unstructured and body-fitted and the spatial discretization is based on a collocated cell-centered variable arrangement. A formally second-order-accurate method is used for time integration of the spatially discretized equations. The PIMPLE algorithm, which is a combination of the PISO [74] (Pressure Implicit with Splitting of Operator) and the SIMPLE [75] (Semi-Implicit Method for Pressure-Linked Equations) algorithms, is used to ensure pressure-velocity coupling while solving for incompressible flow using a collocated variable arrangement.

3.4.2 Dispersed Phase Solver

The time integration of the Lagrangian evolution equations for the dispersed phase given by Eq. (3.1.7) and Eq. (3.1.8) is is performed by using the first-order-accurate Euler scheme where the source terms are treated implicitly. The evolution of the dispersed phase

is performed using the enhanced version of the computationally efficient and robust particle tracking algorithm [76]. For example, new position of the particle $\boldsymbol{x}_p^{n+1}$ is computed from the velocity of the particle at the previous time step $v_{\mathrm{p}i}^n$ through

$$x_{\mathrm{p}i}^{n+1} = x_{\mathrm{p}i}^n + v_{\mathrm{p}i}^n \Delta t_p. \tag{3.4.1}$$

Here, the time step size Δt_p can be different from the flow time step as the particles are tracked from cell to cell by calculating and identifying the face crossings. The face crossing approach is more efficient in the tracking of particles in complex geometries of unstructured, arbitrary polyhedral cells, compared to methods that redetermine the hosting grid cell in every iteration. Therefore a series of individual tracking events can be performed for a flow time step size Δt_f, which ends when the particle crosses a face of a cell or when it arrives at the final destination. The maximum time step used to track a particle is one defined for continuous phase simulation (Δt_f). When the particle reaches a new destination either on a face that has been crossed or at the particle's final destination, the new particle velocity at that point is calculated by integrating Eq. (3.1.8) using the implicit Euler scheme.

CHAPTER 4

DESCRIPTION OF COMPUTATIONAL SETUP AND CASES

In this chapter, first, the test configuration that has been considered is described. Afterward, a description of all the cases considered in this study is presented.

4.1 Computational Setup

To assess the subgrid models and further studies for examining the role of inertia of particles, two-way coupling phenomenon, and polydispersity effects, particle-laden turbulent flow over a backward-facing step is considered in this study. This particular flow configuration has been extensively studied in the past due to its geometrical simplicity, relevance to practical applications, and the presence of a wide range of physical phenomena. It is a canonical flow configuration, which comprises flow features such as near-wall dynamics, separation, reattachment, shear layer, non-equilibrium behavior within the boundary layer after reattachment followed by an approach of the boundary layer towards equilibrium. The numerical investigation of turbulent flow in this configuration at practically relevant Reynolds numbers is challenging to computational approaches. The presence of inertial particles with a loading that leads to a two-way coupling to the turbulent flow increases the complexity. This in turn makes this flow configuration even more challenging for computational models to capture the wide range of flow physics prevalent in this configuration in a reliable and pre-

dictive manner. Due to these reasons, this particular test case has been considered in many past studies leading to the availability of reference data, which can be used for development and assessment studies of computational methods and models.

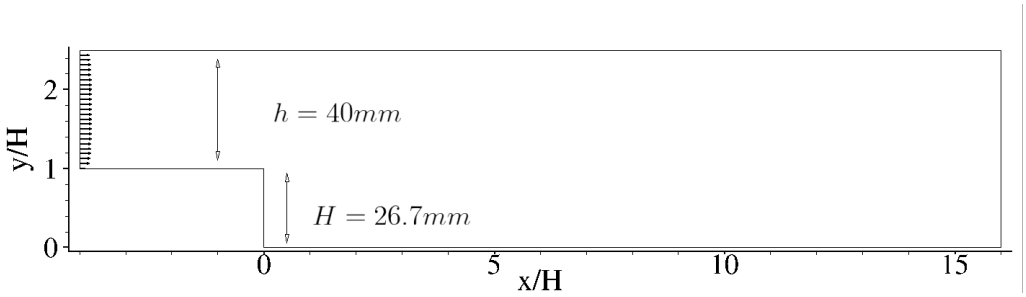

Figure 4.1 A schematic of the configuration used in this study shown in the $x - y$ plane

Figure 4.1 shows a two-dimensional (2D) schematic of the computational domain in the central plane. The extent of the domain is $20H \times 2.50H \times 1.87H$ along the streamwise (x), vertical (y), and spanwise (z) directions. Here, $H = 0.0267$ m is the step height. The extent of the channel length upstream of the step is $16H$. The computational setup follows the past reference studies [7, 33, 77, 78]. In the $x-$direction, an inflow/outflow boundary condition is used. Specifically, at the inflow boundary, a velocity profile corresponding to a fully developed turbulent channel flow with a bulk velocity $U_0 = 10.5$ m/s and a turbulence intensity of 5% is specified. The Reynolds number (Re_{H}) based on the bulk velocity and the step height is 18,400. At the outflow boundary, the homogeneous Neumann condition is specified for the velocity field. A no-slip condition is employed on the top and bottom walls as well as the side walls of the computational domain.

The parameters corresponding to the particles are determined following the past experimental [7] and computational [33] studies. We consider solid spherical copper particles

with a density of 8800 kg/m^3. The particles are injected at the inflow boundary after the carrier phase flow field reaches a statistically stationary state with an injection velocity, which is specified to be 88% of the local carrier phase velocity. The particles are distributed uniformly at the inlet boundary. To examine the effects of Stokes number (St), coupling, and polydispersity, the diameter and mass loading of the particles are varied. The baseline case employed uniformly sized particles of diameter 70 μm with a mass loading of 10% leading to $St = 6.9$ to enable a direct comparison with the reference data. For the particles, walls are treated as rigid boundaries with perfect rebound characteristics and particles are allowed to leave the outflow boundary. As mentioned in Sec. 3.1, the forces acting on the inertial particles include gravity and sphere drag.

4.2 Computational Mesh

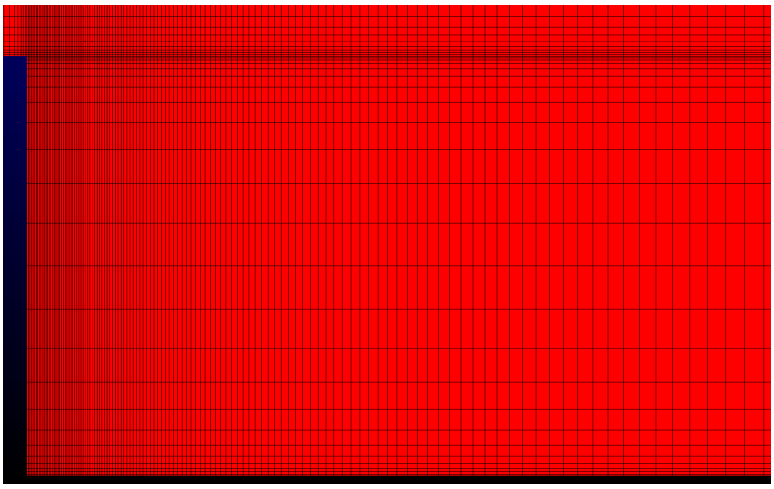

Figure 4.2 The mesh refinement near the step is shown for the coarse mesh

The meshing of the computational domain is performed using the Pointwise software [79]. A close-up view of the computational mesh near the step is shown in Fig. 4.2. The

mesh is refined in the near-wall and shear layer regions to accurately capture the dynamics of turbulence in these regions, which are known to have higher levels of production of turbulent kinetic energy. The grid spacings and number of points are specified following a past numerical study [33]. The vertical spacing constraints near the wall, as well as the vertical and horizontal spacings near the step, are 0.1 mm for all meshes.

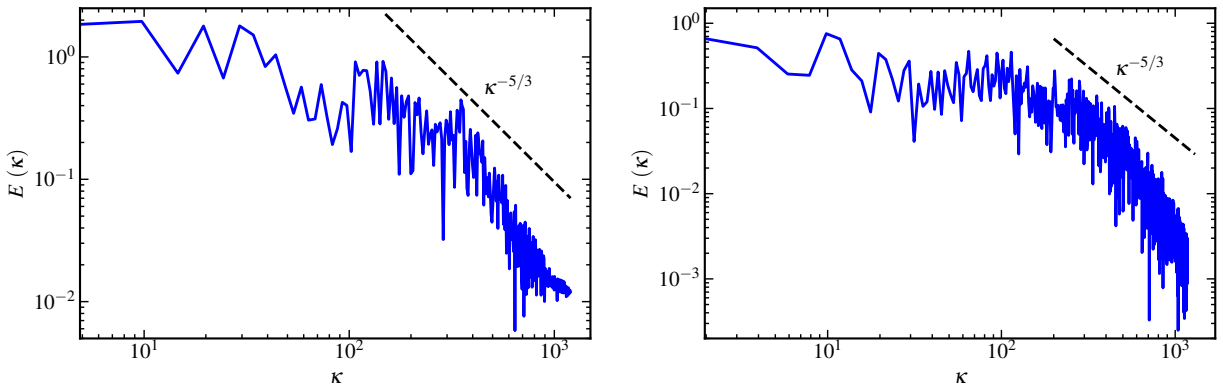

(a) Coarse mesh ($x/H = 5.7, y/H = 0.6$)

(b) Medium mesh ($x/H = 2.7, y/H = 0.7$)

Figure 4.3 Resolved turbulent kinetic energy spectrum in the shear layer region obtained using two different mesh resolutions and at two different grid points located in the central $x - y$ plane

We have considered three different computational grids in this study to assess the grid convergence aspects of the results. These grids comprise 0.26, 0.92, and 2.18 million cells. All of the grids considered in the study can be considered reasonable for performing LES. This is evident from the resolved turbulent kinetic energy spectrum shown in Fig. 4.3, where we can observe with both the grids, that a significant portion of the inertial range showing the presence of the well-known $-5/3^{\text{rd}}$ power-law spectrum is resolved.

Case	SGS Closure	$N_x \times N_y \times N_z$	Processors	Mesh size (M cells)	CPU Time (Hrs)
A_1	No Model	$259 \times 59 \times 20$	14	0.26	46
A_2	LDKM	$259 \times 59 \times 20$	14	0.26	94
A_3	DEVM	$259 \times 59 \times 20$	14	0.26	61
A_4	WALE	$259 \times 59 \times 20$	14	0.26	59
B_1	WALE	$389 \times 91 \times 30$	56	0.92	317
C_1	WALE	$518 \times 119 \times 40$	56	2.18	1140

Table 4.1 Simulation parameters for unladen cases considered in this study

4.3 Description of Cases

A wide range of test cases are considered in this study to examine grid convergence, assess different types of subgrid models, and perform further applications studies. The first set of cases are referred to as unladen cases (no particles), which are used to perform the grid convergence study and to identify the best performing subgrid-scale (SGS) closure model for this particular test configuration. The simulation parameters for these cases are summarized in Table 4.1. The assessment of the performance of the closure models for the SGS stress tensor is carried out using a coarse grid, as the SGS model contribution tends to be higher on coarser grids. A no-model case is also considered to demonstrate the effects of the inclusion of the SGS models. After identifying the best performing SGS closure, a grid convergence study with this model is performed using three different grid sizes comprising 0.26 M, 0.92 M, and 2.18 million cells.

The second set of cases include the particle-laden flows, which are used to assess

Case	Coupling	Disp. Model	St	CPUs	Φ_m	Cells (M)	CPU Time (Hrs)
D_1	One-way	None	6.9	14	0.08	0.26	129
E_1	Two-way	None	6.9	14	0.10	0.26	172
E_2	Two-way	None	6.9	14	0.20	0.26	147
E_3	Two-way	RW	6.9	14	0.10	0.26	127
F_1	Two-way	None	6.9	56	0.10	2.18	1060
F_2	Two-way	DF	6.9	56	0.10	2.18	1150
F_3	Two-way	RW	6.9	56	0.10	2.18	1120
G_1	Two-way	RW	0.1	28	0.20	0.92	881
G_2	Two-way	RW	1.0	28	0.20	0.92	847
G_3	Two-way	RW	6.9	28	0.20	0.92	826
G_4	Two-way	RW	10.0	28	0.20	0.92	826
H_1	One-way	RW	1.0	56	0.01	0.92	1280
H_2	One-way	RW	1.0	56	0.20	0.92	1450
H_3	Two-way	RW	1.0	56	0.20	0.92	1540
I_1	Two-way	RW	1.0	56	0.20	0.92	1510
I_2	Two-way	RW	1.0	56	0.20	0.92	1540

Table 4.2 Simulation parameters for particle-laden cases considered in this study

subgrid dispersion models while using the WALE model for the SGS stress tensor. Apart from assessing the performance of subgrid dispersion models, additional cases are simulated to examine the effects of St, two-way coupling, and polydisperse distribution of particles. The number of particles simulated in each case is approximately 100k for Case D_1, 130k for the cases with mass loading of 0.10, and 260k for the cases with mass loading of 0.20. Gravity was turned off for Case D_1 because it was an initial test case to determine that the parameters were defined properly. In particular, $St = 0.1$, 1, 6.9, and 10 have been considered to examine the role of particle inertia. Note that for $St \ll 1$, particles tend to behave as tracer particles that follow the carrier phase, whereas for $St \gg 1$, the particles tend to not respond to the carrier phase. The baseline case corresponds to $St = 6.9$ for which reference results are available for comparison. To examine the effect of particle-to-fluid coupling effects, mass loadings of 0.01, 0.1, and 0.2 have been considered. To assess polydispersity effects, additional cases corresponding to the conditions of the baseline case have been considered, where the mean diameter of the particles is specified to be the same as the baseline case with a standard deviation of 8.66% of the mean value. We have considered uniform and normal distribution to examine the effects of polydispersity.

All the simulations have been evolved for 4 flow-through times to allows for initial transients to pass and establish a statistically stationary state of the turbulent flow field. Afterward, time-averaged statistics of the carrier and dispersed phases are obtained by simulating for an additional 10 flow-through times. Some of the cases have been simulated even longer to ensure converged statistics of the flow field.

The simulations have been carried out in parallel using the HPC resources facilitated by the SimCenter at UTC.

CHAPTER 5

ASSESSMENT OF SUBGRID MODELS

This chapter presents the results from the LES of unladen and particle-laden cases, where the focus is on the assessment of the subgrid models considered in this study. The subgrid models are used to attain closure of the SGS stress tensor in the governing equations for the carrier phase, and the subgrid dispersion in the evolution equations for the dispersed phase. First, the assessment of the models for the SGS stress tensor is discussed in Sec. 5.1, which is accomplished by simulating the unladen cases using a coarse grid. Afterward, a grid convergence study is discussed in Sec. 5.2 to identify the optimal grid with the chosen model for the SGS stress tensor. Afterward, the assessment of subgrid dispersion models is discussed in Sec. 5.3. Finally, a summary of the optimally performing modeling strategy is presented in Sec. 5.4. The performance of models is examined by comparing the results from the simulations with the available reference results [7, 33].

5.1 Subgrid-Scale Stress Model Assessment

We consider three well-established eddy viscosity-based closure models for the SGS stress tensor. These include the dynamic eddy viscosity model (DEVM), the wall-adapting local eddy-viscosity model (WALE), and the one-equation-based locally dynamic kinetic energy model (LDKM). Additional preliminary simulations with the classical Smagorinsky and

the constant-coefficient one-equation-based model showed underperformance of these models, and therefore, the results from these models are not included. An additional simulation was also performed, which did not use any SGS model to show the effects of the use of a closure model. The predictive capabilities of the closure models are assessed in the terms of comparison of the first- and second-order turbulence statistics of the streamwise velocity, and the reattachment length. The profiles of the mean streamwise velocity and its intensity are compared at four streamwise locations from the step, which are located at $x/H = 2$, 5, 9, and 14. These locations are indicated in Fig. 5.1, which shows the contours of the time-averaged streamwise velocity in the central $x - y$ plane overlaid with the streamlines obtained from the case employing the WALE model. Immediately downstream of the step, a sudden expansion of the flow causes separation and subsequent reattachment on the bottom wall. This, in turn, leads to the presence of a primary corner recirculation zone. We can also observe a small recirculation zone on the top wall and a secondary recirculation zone at the step corner on the bottom wall. Qualitatively, all the models show a similar type of mean flow behavior. Next, we discuss the comparison of the time-averaged profiles of the streamwise velocity and its intensity.

Figure 5.2 shows a comparison of the wall-normal profile of the normalized mean streamwise velocity obtained using different models at four streamwise locations. The results are compared with the reference experimental data [7]. As stated before, all the LES cases employ the same coarse grid and same numerical method, thus illustrating a direct comparison of the effects of the employed SGS model. Overall, all the four LES cases yield

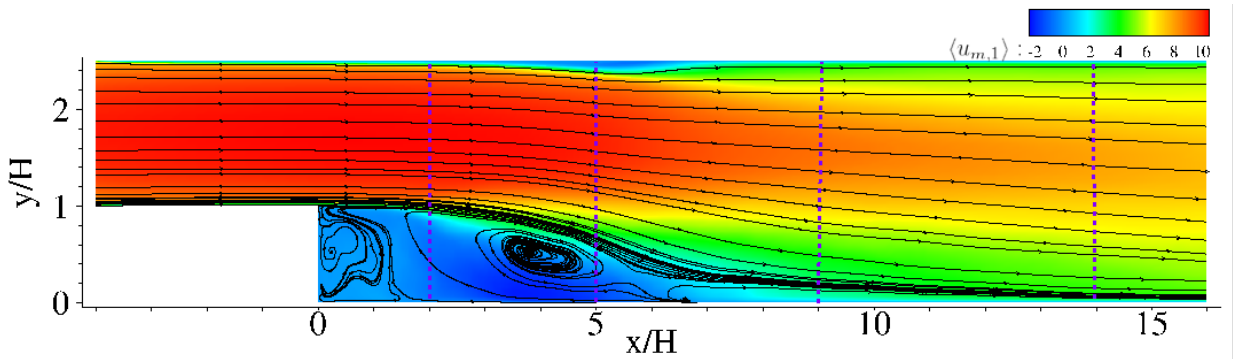

Figure 5.1 Contours of time-averaged streamwise velocity overlaid with streamlines obtained from the unladen case with WALE as the SGS model. The four streamwise locations are also indicated where profiles are compared with the experimental profiles

similar results, where a reasonable agreement with the reference experimental profile can be observed at $x/H = 2$. Similar to the experimental case, a backflow indicating the presence of recirculating zone at this location is evident. Furthermore, a good agreement is observed in the profile near the top wall. Some differences from the experiment are evident in terms of a lower spreading of the shear layer and lower magnitude of the backflow velocity. A similar reasonable agreement is also evident at $x/H = 5$ with deviations notable in the lower half of the channel. However, further downstream, although all the closure models yield similar profiles, the agreement with the experimental profile tends to decrease. The increased level of differences can be attributed to the differences within the shear layer region observed at $x/H = 2$, which affects the turbulent mixing and transport, and thus the characteristics of the spatial development of the flow at downstream locations. Similar types of differences between LES and experiments have been reported in the past studies of flow over a bluff body [80] and flow over a backward-spacing step [33, 77, 81].

A further comparison of the results from different modeling approaches is carried

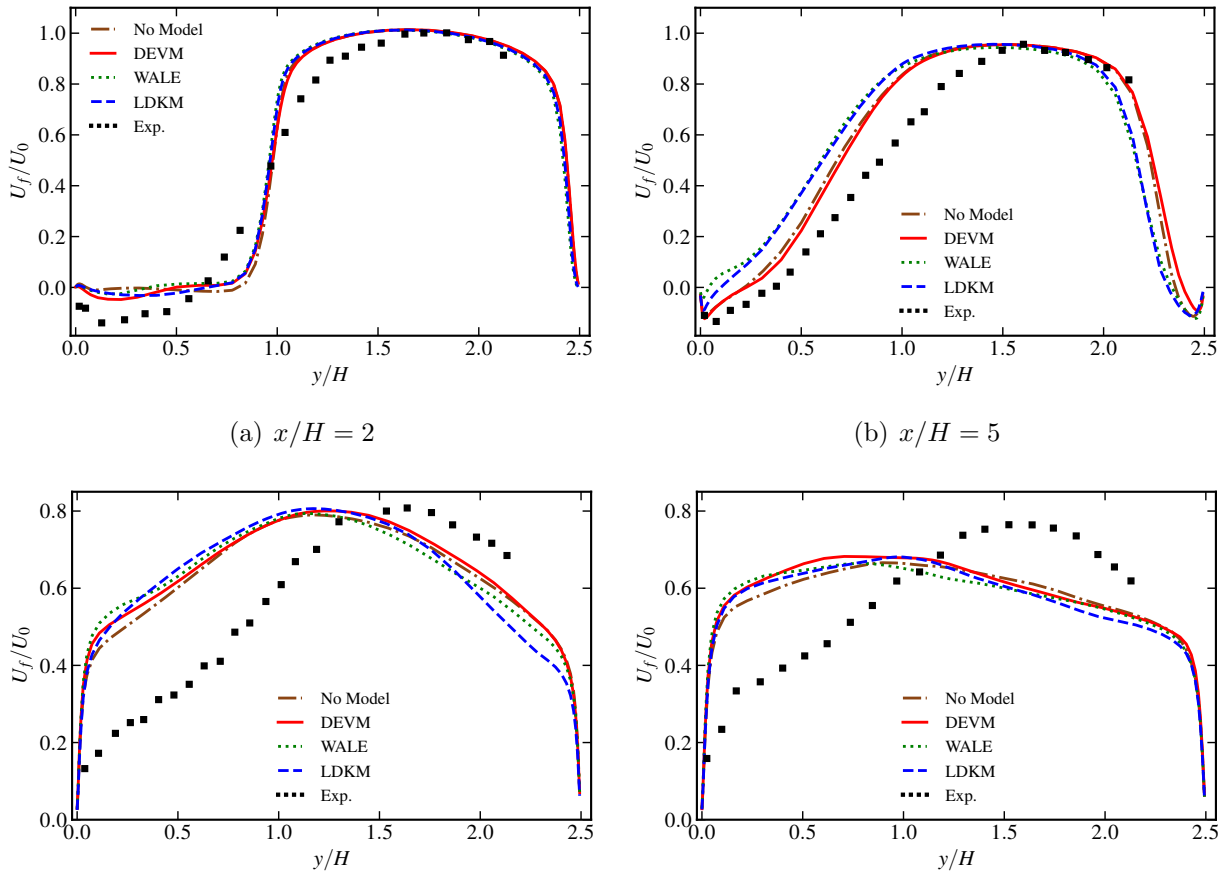

(a) $x/H = 2$ (b) $x/H = 5$

(c) $x/H = 9$ (d) $x/H = 14$

Figure 5.2 Normalized streamwise mean velocity profile at four streamwise locations downstream of the step obtained from cases using different SGS stress models and compared with the experimental results

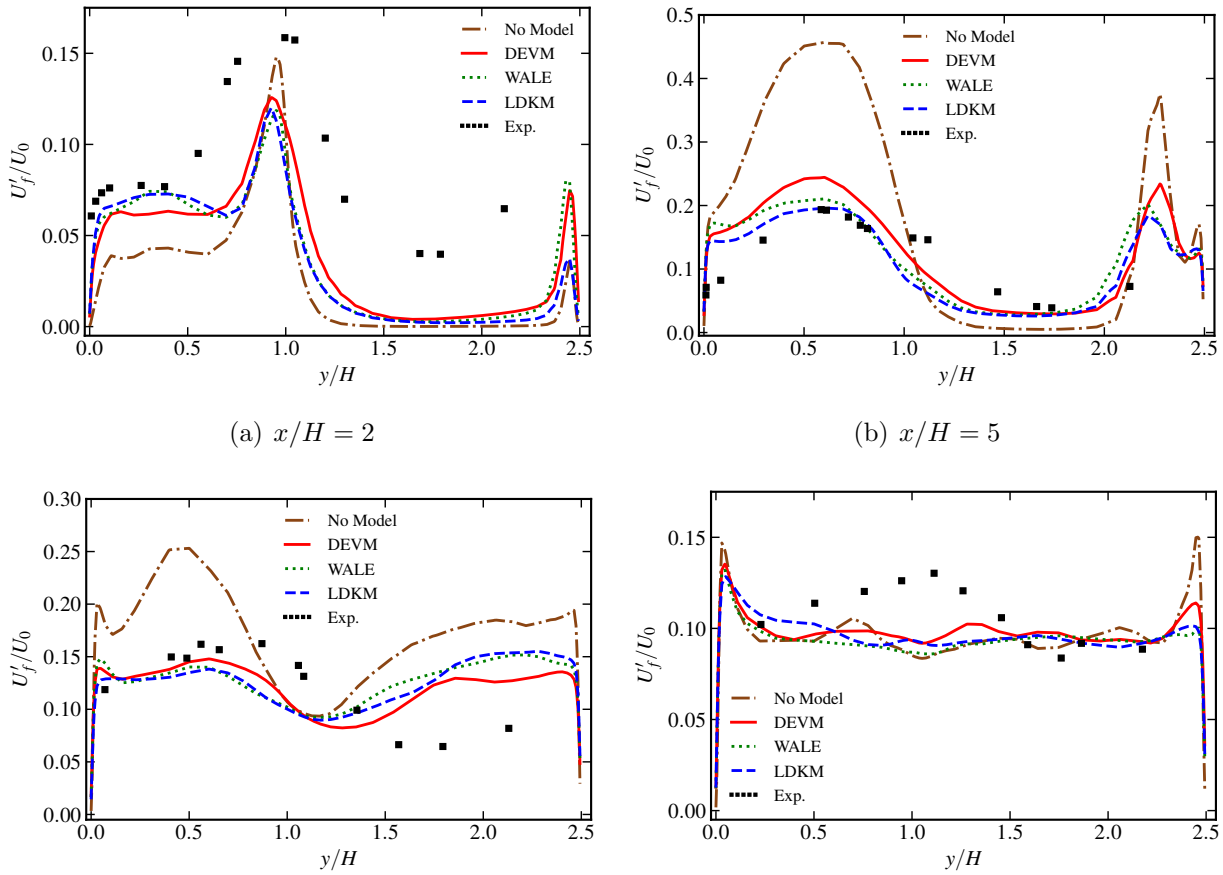

(a) $x/H = 2$

(b) $x/H = 5$

(c) $x/H = 9$

(d) $x/H = 14$

Figure 5.3 Profile of normalized streamwise intensity at four streamwise locations downstream of the step obtained from different SGS stress models and compared with the experimental profile

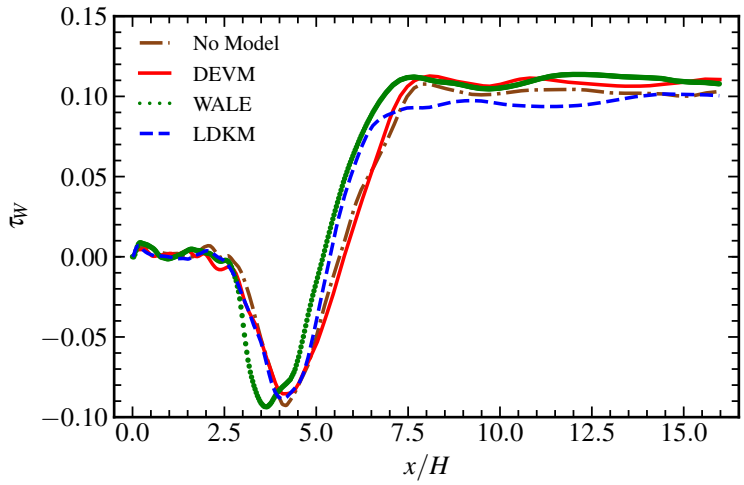

Figure 5.4 Wall shear stress distribution on the bottom wall for the unladen cases comparing different SGS models

out in the terms of the wall-normal profile of the streamwise turbulence intensity, which is shown in Fig. 5.3. It is evident from these figures that the no-model approach yields different results compared to the other models as well as reference experimental data. At $x/H = 2$, it underpredicts the values of the streamwise intensity by about 99% in the lower part of the channel. On the other hand, the no-model overpredicts the intensity at $x/H = 5$ and $x/H = 9$ in the lower part of the channel by 220% and 67%, respectively. These results clearly show the need for the SGS model. At all the locations both WALE and LDKM approaches yield similar and better results compared to the DEVM approach, particularly up to $x/H = 9$ and in the lower half of the channel. The differences with the experimental results by all the models are related to the spatial evolution of the shear layer, which tends to differ between the simulation and experiments as shown before in Fig. 5.2.

The performance of the models is now assessed in terms of the prediction of the mean reattachment length x_{R}, which is defined in terms of the change in the sign of the wall shear

stress (τ_w) on the bottom wall. The streamwise profile of τ_w from the four cases are shown in Fig. 5.4. The reattachment length from these simulations is summarized in Table 5.1. All the cases underpredict the reattachment length in comparison to the experimental value of 7.4 [7]. It is shown later in Sec. 5.2 that the refinement of the grid leads to an improved prediction of the values of x_R. We can observe that no-model and DEVM lead to higher values of x_R compared to the other two models. This can be attributed to a higher level of dissipation in the WALE and LDKM on the coarse mesh [80]. However, we have already observed that both no model and DEVM showed higher levels of discrepancy in the prediction of the streamwise intensity (see Fig. 5.3), particularly in the lower half of the channel.

Table 5.1 Time averaged reattachment length (x_R) in the central plane comparing the cases employing different SGS models

Case	SGS Model	x_R/H
A_1	None	5.6
A_2	LDKM	5.4
A_3	DEVM	5.8
A_4	WALE	5.2
Exp.	-	7.4

Based on the results shown in this section, we can observe that both WALE and LDKM yields comparable results on the baseline coarse grid. However, we consider the WALE model for further studies as compared to DEVM and LDKM, it is computationally

efficient. This is due to the algebraic formulation employed by WALE in comparison to a dynamic approach in DEVM and the cost associated with solving an additional transport equation and dynamic procedure in the LDKM approach. Specifically, the cost (in CPU hours) per flow-through time is 4.7, 5.9, 6.1, and 9.4 for cases with no-model, WALE, DEVM, and LDKM as SGS closures, respectively.

5.2 Grid Convergence Study

In this section, a grid convergence study is performed for the unladen cases where WALE is used as a model for the SGS stress tensor. The baseline coarse grid considered here followed a past LES study [33]. We consider two other grids referred to as medium and fine grids in this study to demonstrate the grid convergence aspect of the results. The total number of cells is 0.26 M in the coarse grid. The medium and fine grids are obtained by increasing the number of points in each direction by a factor of 1.5 and 2, respectively, leading to 0.92 M and 2.18 M cells in these cases.

Figure 5.5 shows the wall-normal profile of the mean streamwise velocity at the four streamwise locations. We can observe an improvement in the agreement with the experimental profiles as the grid is refined. The improvement is particularly noticeable at locations further downstream of the step. Although the improvement from the coarse to the medium grid is significant, the improvement from the medium to the fine grid is moderate, thus indicating the adequacy of the medium grid. The improvement in the prediction of the streamwise turbulence intensity as the grid is refined is also evident from Fig. 5.6. The medium grid results as expected are better compared to the coarse grid case, particularly at

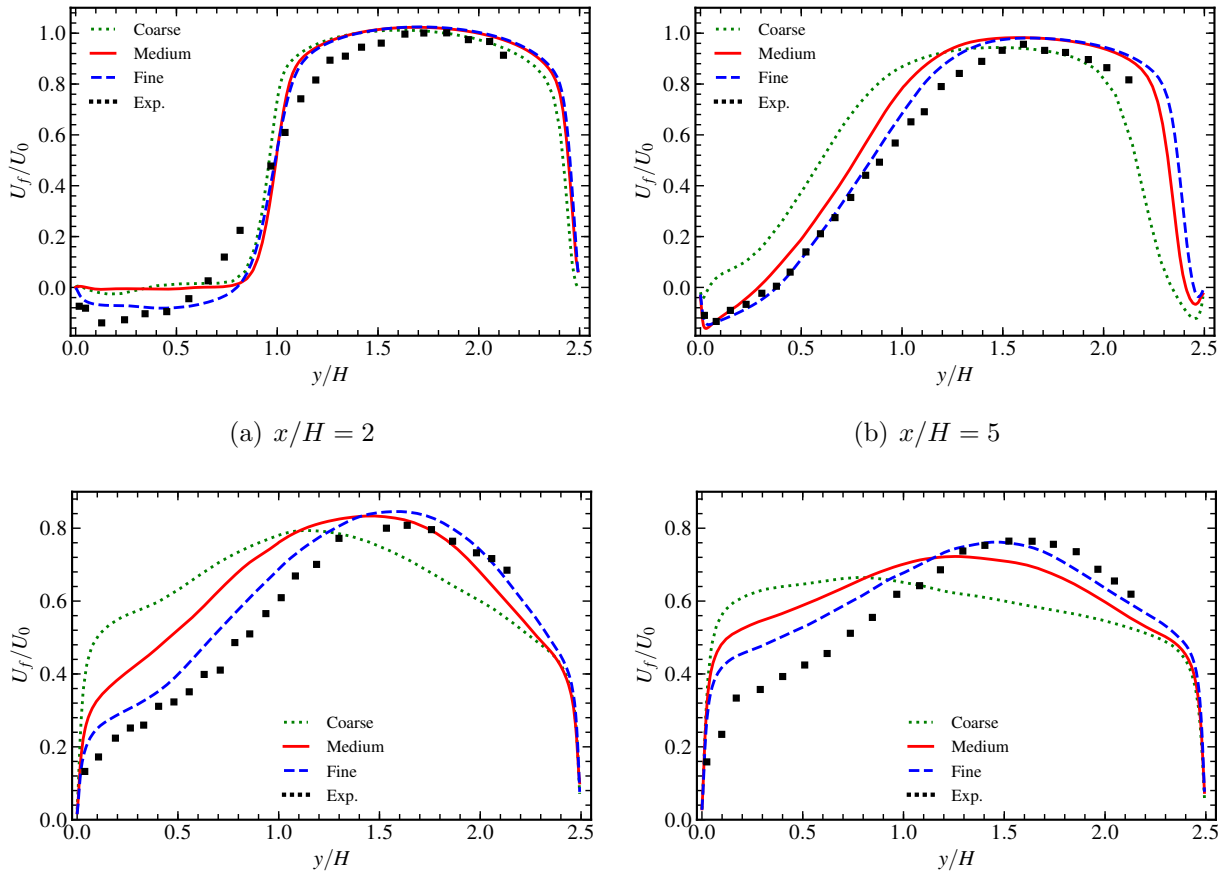

(a) $x/H = 2$

(b) $x/H = 5$

(c) $x/H = 9$

(d) $x/H = 14$

Figure 5.5 Normalized streamwise mean velocity profile at four streamwise locations downstream of the step obtained from different meshes and compared with the experimental profile

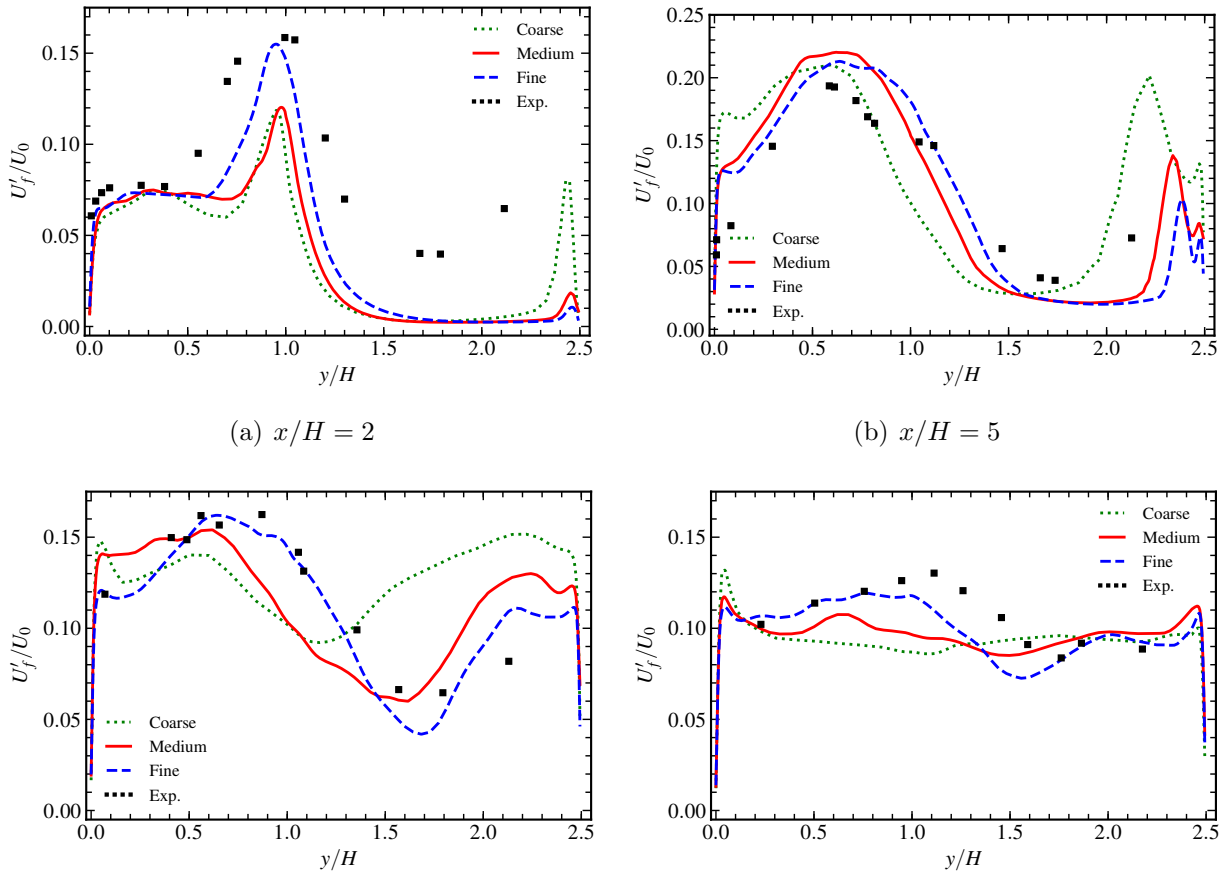

(a) $x/H = 2$ (b) $x/H = 5$

(c) $x/H = 9$ (d) $x/H = 14$

Figure 5.6 Profile of normalized streamwise intensity at four streamwise locations downstream of the step obtained from different meshes and compared with the experimental profile

the downstream locations.

The significant improvements in the prediction of the first- and second-order turbulence statistics as the grid is refined from coarse to medium sized is also noted in the variation of the wall shear stress profile on the bottom wall in the central $x - y$ plane, which is shown in Fig. 5.4. The size of the recirculation zone is smaller in the coarse grid compared to the other two grids. Quantitatively, x_R/H is 5.2, 6.2 and 6.6 for the coarse, medium and fine grid cases, respectively.

Based on the results in this section, we can infer that as the grid is refined, the agreement with the experimental results tend to improve, albeit at an increased computational cost. Since the medium grid showed improved predictions compared to the coarse grid for the first- and second-order statistics and its computational cost is only about 30% of the corresponding fine grid case, it has been chosen to perform further studies.

5.3 Subgrid Dispersion Model Assessment

We consider two dispersion models, namely, the stochastic random walk (RW) model and the spatially uniform differential filter (DF) model, to assess the role of subgrid dispersion models. Both these cases are simulated using the fine mesh. These cases are simulated at $St = 6.9$ and $\Phi_{\mathrm{m}} = 0.1$ to facilitate a direct comparison with reference results. An additional case with no subgrid dispersion model is also simulated to examine if the inclusion of a subgrid

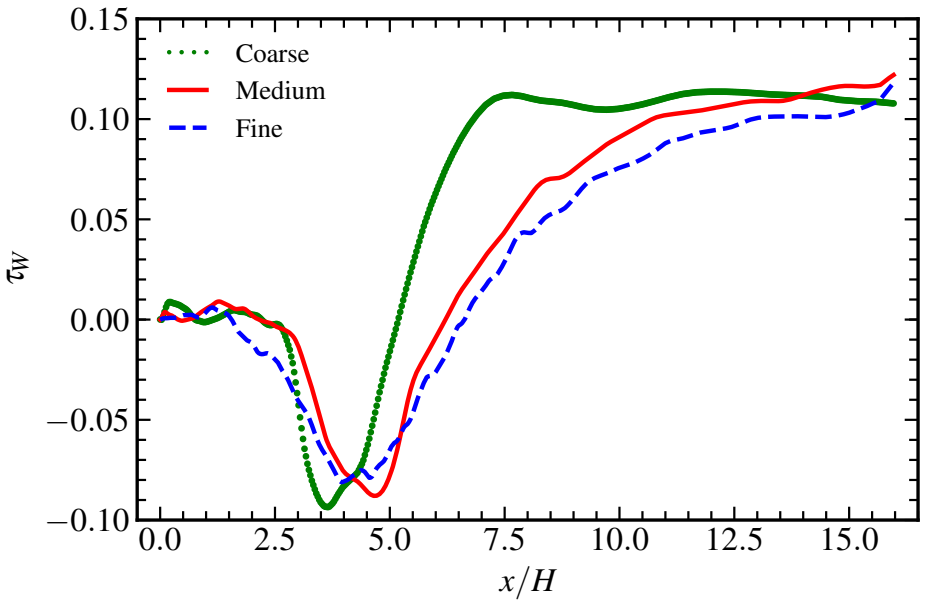

Figure 5.7 Wall shear stress distribution on the bottom wall for the unladen cases comparing different computational meshes

dispersion model improves the agreement with the reference results.

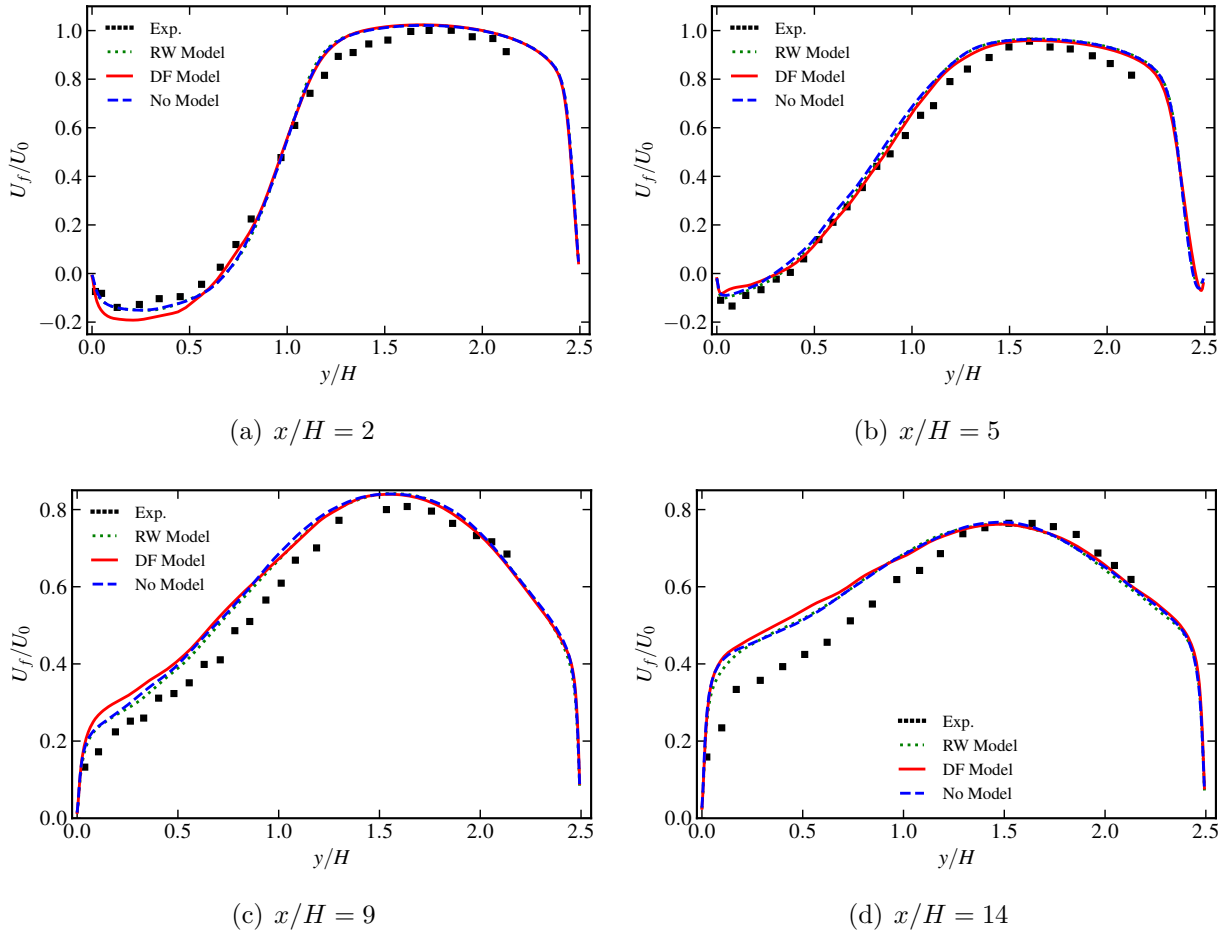

(a) $x/H = 2$ (b) $x/H = 5$

(c) $x/H = 9$ (d) $x/H = 14$

Figure 5.8 Normalized streamwise mean velocity profile at four streamwise locations downstream of the step obtained from different subgrid dispersion models and compared with the experimental profile

The wall-normal profile of the mean streamwise velocity comparing the cases employing different subgrid dispersion models with the experimental data is shown in Fig. 5.8 at the four different streamwise locations. We observe a very small sensitivity of the mean velocity profile to the subgrid dispersion models at all the locations. The results from RW and no-model tend to overlap and are slightly better compared to the profile obtained using the DF

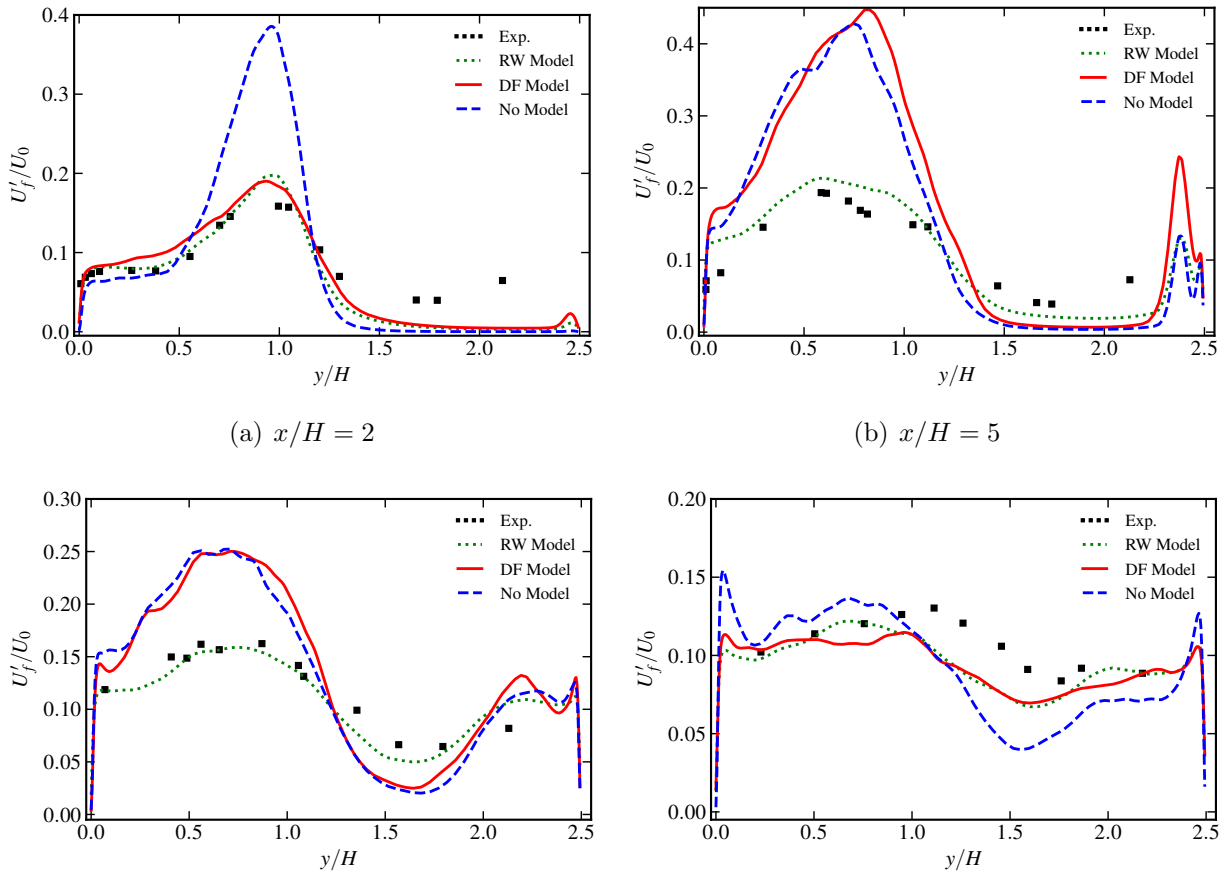

(a) $x/H = 2$

(b) $x/H = 5$

(c) $x/H = 9$

(d) $x/H = 14$

Figure 5.9 Profile of normalized streamwise intensity at four streamwise locations downstream of the step obtained from different subgrid dispersion models and compared with the experimental profile

model, particularly, in the lower half of the channel. However, the prediction of the profiles of the streamwise intensity is in very good agreement with the reference data compared to the DF and no-model approaches, which is evident from Fig. 5.9. The improved predictions by the RW model in comparison to the no-model approach clearly illustrate the importance of the inclusion of a subgrid dispersion model. Additionally, a better prediction at all the locations compared to the DF model demonstrates the superiority of the RW model, at least for this particular test configuration. A better agreement with the results by using the RW model is also evident from the prediction of the mean reattachment length, which from the

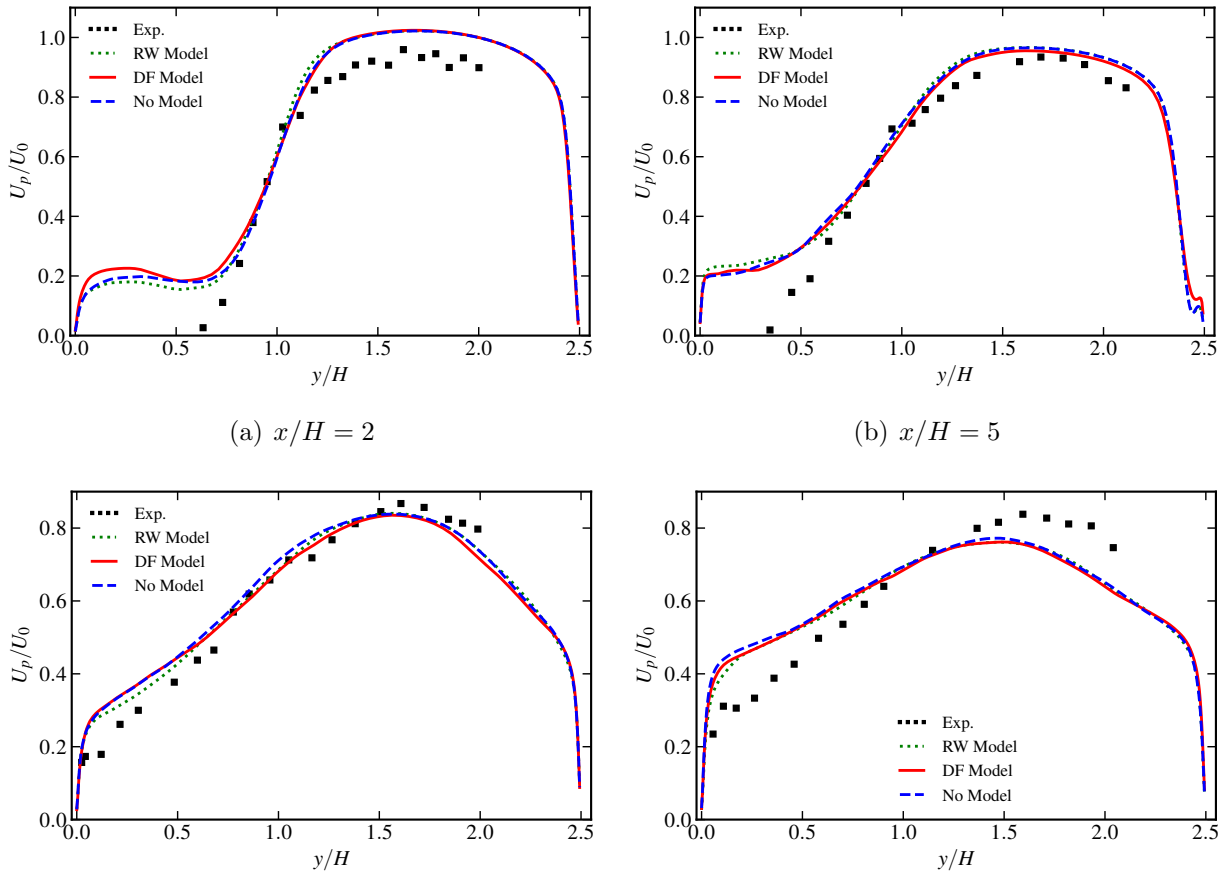

(a) $x/H = 2$

(b) $x/H = 5$

(c) $x/H = 9$

(d) $x/H = 14$

Figure 5.10 Normalized streamwise mean velocity profile of the dispersed phase at four streamwise locations downstream of the step obtained from different subgrid dispersion models and compared with the experimental profile

cases employing no-model, DF, and RW models is 6, 5.9, and 6.4, respectively, in comparison to 7.4 from the experiments.

Similar to the profiles of the mean streamwise velocity of the carrier phase, the wall-normal variation of the mean streamwise velocity of the dispersed phase shows minor sensitivity to the employed subgrid dispersion model, which is evident from Fig. 5.10. However, the sensitivity of the profiles of the mean streamwise intensity to the subgrid dispersion model is enhanced as can be observed from Fig. 5.11. This is particularly evident at far

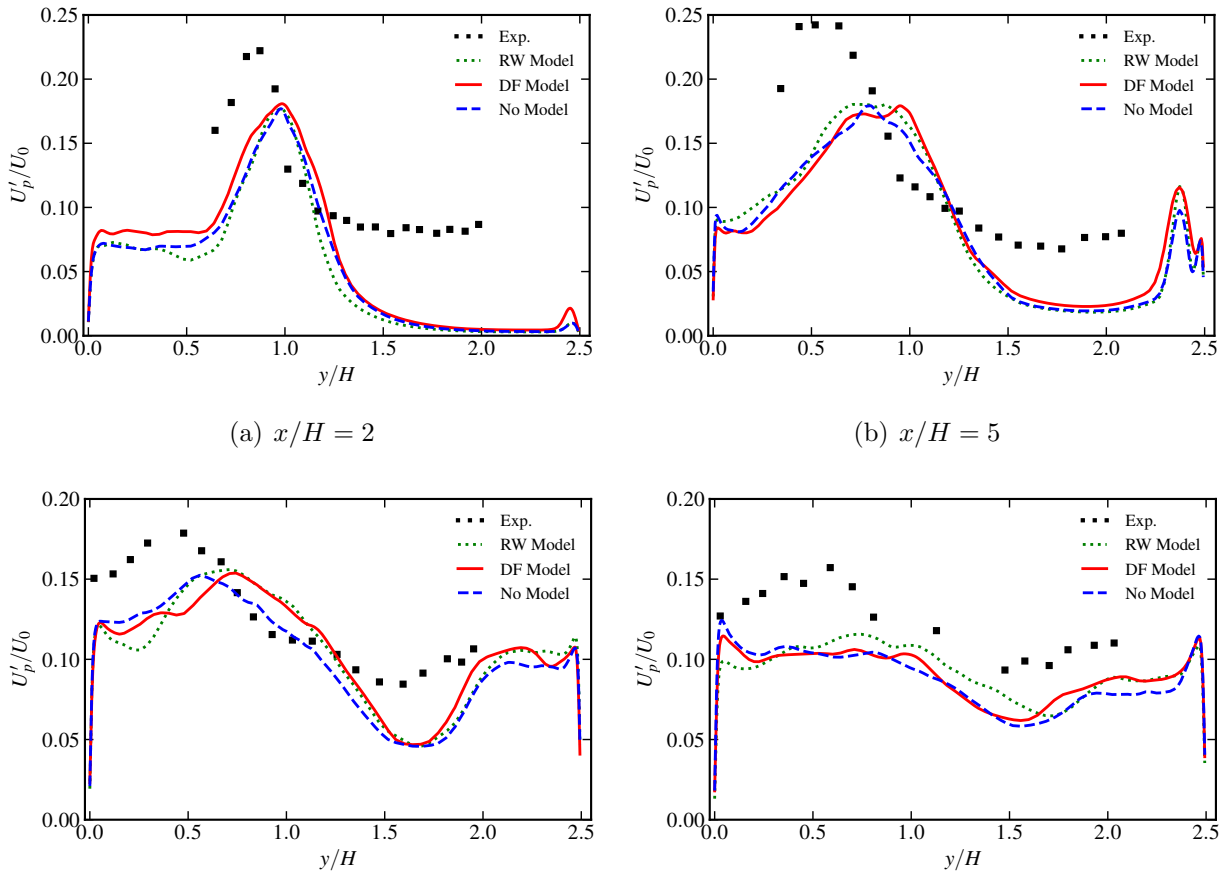

(a) $x/H = 2$

(b) $x/H = 5$

(c) $x/H = 9$

(d) $x/H = 14$

Figure 5.11 Profile of normalized streamwise velocity fluctuations of the dispersed phase at four streamwise locations downstream of the step obtained from differerent subgrid dispersion models and compared with the experimental profile

downstream locations, i.e., for $x/H > 5$. All the cases show significant differences compared to the reference results, which can be attributed to discrepancies in the prediction of the carrier phase flow field at the resolved level. At downstream locations, the cases which utilize a subgrid dispersion model yield an increase in the intensity of the velocity of the dispersed phase, which is still lower than the reference results, yet is better compared to the no-model approach. In the core region of the channel, the RW model tends to produce a higher fluctuation compared to the DF model, especially at far downstream locations.

Overall, the results in this section demonstrate that the use of a subgrid dispersion model yields improved prediction of statistical features of the carrier phase flow field. There are differences in the prediction of the statistics of the dispersed phase, which perhaps is associated with the resolved field. Therefore, the inclusion of the subgrid dispersion model only leads to minor improvements in the statistics, particularly, at downstream locations.

5.4 Summary

In this chapter, we carried out a detailed assessment of the predictive capabilities of different modeling approaches for LES of two-way coupled particle-laden turbulent flow over a backward-facing step. The assessment is performed in terms of comparison of the first- and second-order statistics of the carrier and dispersed phases with the available reference results. Based on the assessment of subgrid models, grid convergence, and computational cost, we conclude that the WALE model for closure of the SGS stress tensor and stochastic RW model for closure of the subgrid dispersion on the medium-sized grid can be considered

optimal for LES-based further studies of this particular flow, which is discussed in the next chapter.

CHAPTER 6

EFFECTS OF INERTIA, COUPLING, AND POLYDISPERSITY

In this chapter, the effects of inertia of particles, particle-to-fluid coupling, and polydisperse distribution of particles on the features of the carrier and dispersed phases are examined. All the simulations considered in this chapter employ the medium-sized computational mesh (0.92 M cells) and use WALE and RW closures for the modeling of the SGS stress and subgrid dispersion, respectively. First, a qualitative description of the three-dimensional instantaneous flow field is provided in Sec. 6.1. Afterward, the results from a variation of Stokes number, which characterizes the inertia of particles are presented in Sec. 6.2. Next, the effects of particle-to-fluid coupling are analyzed in Sec. 6.3. Finally, the results from a polydisperse distribution of particles are examined in Sec. 6.4 by comparing with the monodisperse distribution of particles.

6.1 Description of Flow Field

Figure 6.1 (a) shows the iso-surfaces of the Q-criterion corresponding to the carrier phase flow field at an arbitrary time instant to illustrate the key 3D flow features. We can observe the formation of a shear layer with intense vorticity immediately downstream of the step corner. The sudden expansion of the flow causes an adverse pressure gradient, which results in the separation of the flow. This is evident from the negative values of the velocity

adjacent and downstream of the step. The flow reattaches further downstream, after which it tends to approach towards fully developed flow in a channel. Similar to wall-bounded turbulent flow in a channel, intense vortical activity is observed in the near-wall regions.

The spatial distribution of the dispersed phase in 3D, colored by their spanwise position is shown in Fig. 6.1 (b). The effects of turbulence of the carrier phase and gravity are noticeable. Particles tend to distribute away from the recirculating region and approach the lower wall further downstream due to the gravity force. At further downstream locations, the dispersion in the wall-normal direction enhances, again illustrating the role of the turbulent carrier phase flow field.

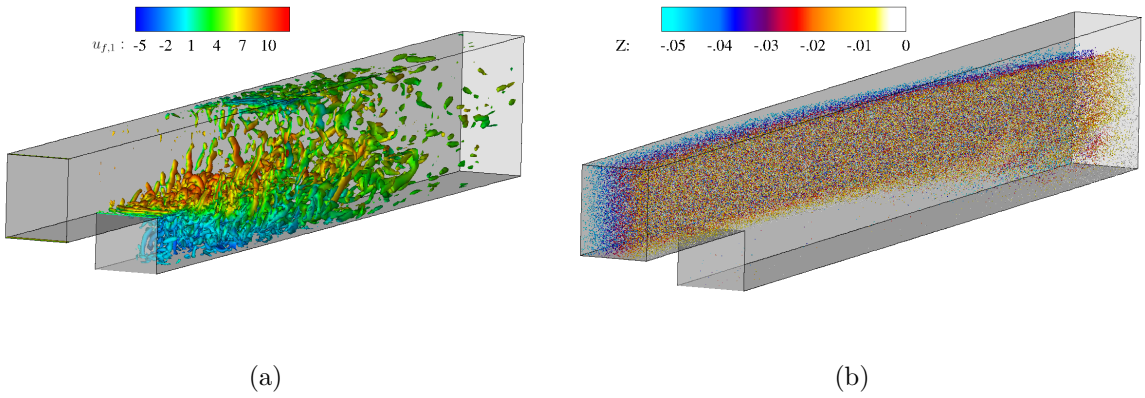

(a) (b)

Figure 6.1 Iso-surfaces of the Q-criterion ($Q = 200,000$) colored by the carrier phase streamwise velocity (a) and the spatial distribution of particles colored by spanwise position (b) both obtained from the two-way coupled case with $St = 6.9$ at $\Phi_{\mathrm{m}} = 0.2$

6.2 Effect of Stokes Number

The Stokes number (St) is defined as a ratio of the characteristic time scale of the dispersed and the carrier phases, i.e., $St = \tau_{\mathrm{p}}/\tau_{\mathrm{f}}$. Therefore, for a fixed characteristic time scale of the carrier phase τ_{f}, changing St implies a change in τ_{p}, which is related to the

inertia of the particles. In particular, particles with smaller values of St ($\ll 1$) tend to follow the carrier phase, whereas particles with larger values of St ($\gg 1$) tend to be unresponsive to the local variations of the carrier phase dynamics. To examine the effects of inertia of particles, we have simulated cases with St of 0.1, 1, 6.9, and 10 at a mass loading $\Phi_{\mathrm{m}} = 0.2$. The change in St is attained by modifying the diameter of the mono-dispersed particles. Note that the case $St = 6.9$ corresponds to the reference experiments.

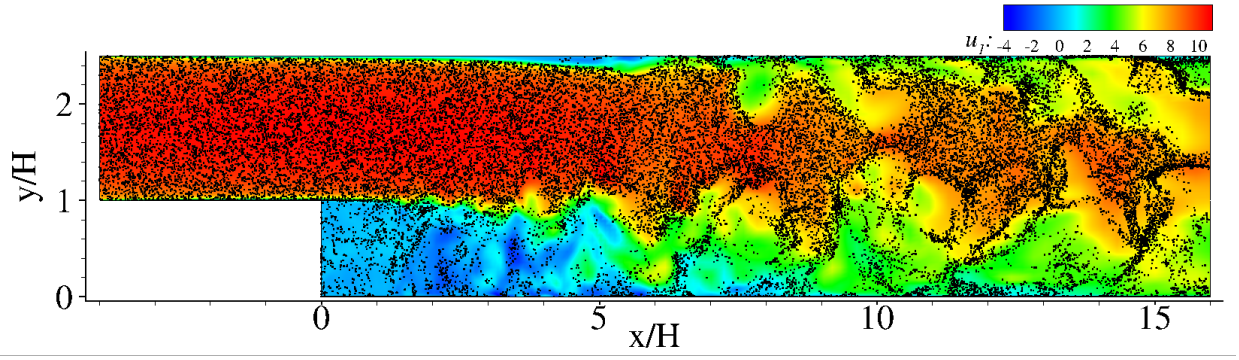

(a) $St = 0.1$

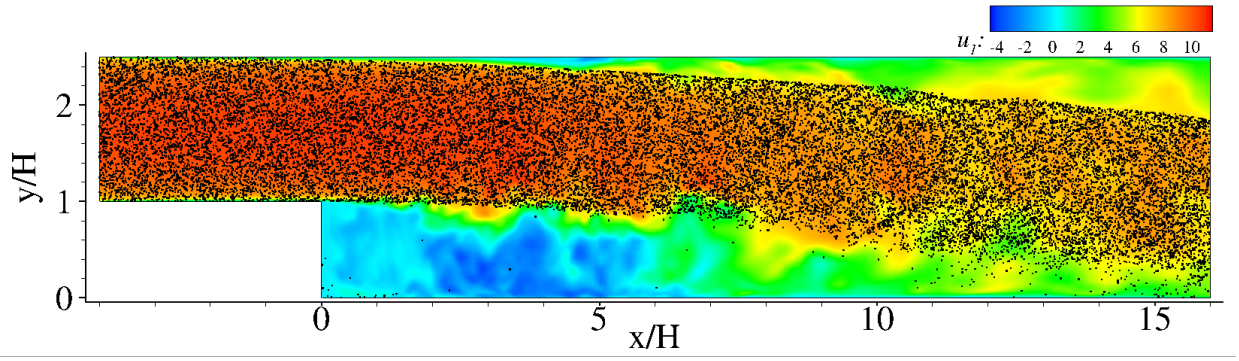

(b) $St = 10$

Figure 6.2 Contours of instantaneous carrier phase streamwise velocity overlaid with the spatial distribution of particles for cases with $St = 0.1$ and 10

Figure 6.2 shows the contours of the instantaneous streamwise velocity in the central $x - y$ plane, where the distribution of particles is also shown. The effect of St on the spatial

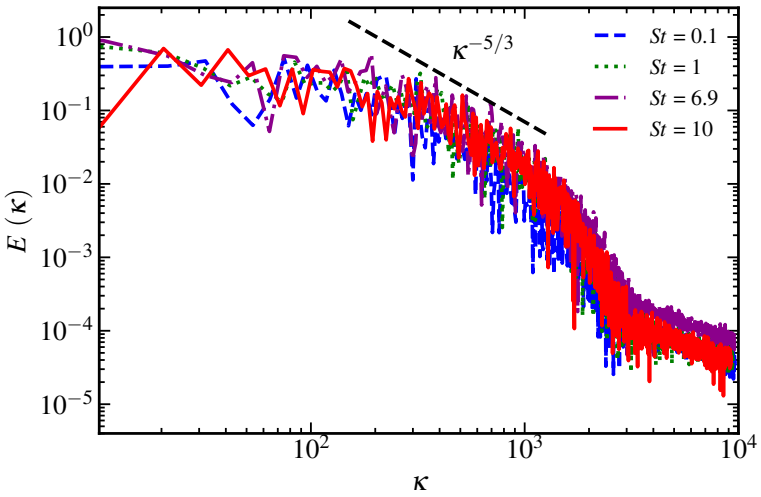

Figure 6.3 Resolved turbulent kinetic energy spectrum from the cases with different Stokes numbers at location ($x/H = 2.74,\ y/H = 0.75$) in the central $x - y$ plane

distribution of particles is clearly evident. In the case with $St = 0.1$, the particles tend to follow the local fluctuations in the carrier phase, thus highlighting the range of scales of motion prevalent in the carrier phase flow field. However, at $St = 10$, the spatial distribution of particles behave much differently, where the dynamics of particles are mainly affected by their inertia and the gravity force. The behavior of the distribution of particles in cases with $St = 1$ and 10 is transitional from low to high St, where the particles tend to follow the large-scale flow features. These observations are consistent with the past studies, which have shown that particles with low St act as tracers [9], and intermediate to high St particles behave ballistically to the carrier flow field [63].

Further analysis of the resolved turbulent kinetic energy (TKE) spectrum at a location in the shear layer at different Stokes numbers shows the effect of Stokes number on the resolved energy, especially in the inertial regime. This is exhibited in Figure 6.3, with the increased St cases resolving a higher energy level here.

The particle number density was computed using a three-dimensional binning approach in the central plane of the channel to determine the number of particles in each bin. The particles within one grid spacing of the central x-y plane past the step were analyzed. The lower left corner had at least an order of magnitude more particles than the mean value in the channel, so these points were skipped. For the $St = 0.1$ case, the particles on the bottom wall were skipped all together for this same reason. Then, the count of particles was normalized by the total number of particles in the bin. Next, the data was loaded in Tecplot [82] and multiple time files were averaged to eliminate instantaneous clustering. Finally, the number density was normalized by the maximum value in a single bin to obtain a range of 0 to 1. The normalized particle number density contours, shown in Figure 6.4 for the low, intermediate, and high Stokes numbers show the differences in dispersion for cases with different particle inertia. The low St case shows nearly a uniform distribution, with the exception of the small-to-moderate sized clusters. As the Stokes number increases, the particles tend to concentrate towards the center of the channel, instead of preferentially concentrating in clusters.

The effects of variation in St on the carrier phase are examined now in terms of the time-averaged statistics. Figure 6.5 shows the contours of streamwise velocity in the central plane for the cases with $St = 0.1$ and 10. Qualitatively, in both cases, the flow features are similar, which shows the presence of a primary recirculation zone on the bottom wall, a shear layer, a smaller recirculation zone on the top wall, and the approach of the flow towards a conventional channel flow after reattachment. However, some differences are

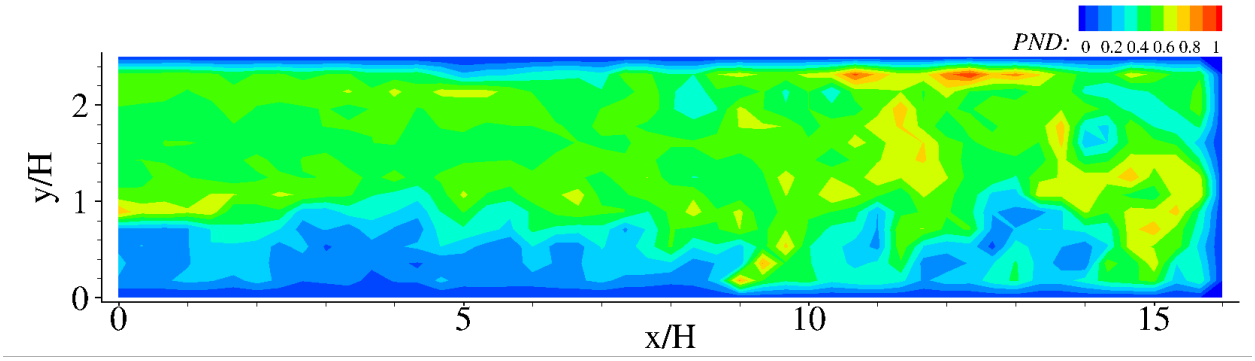

(a) $St = 0.1$

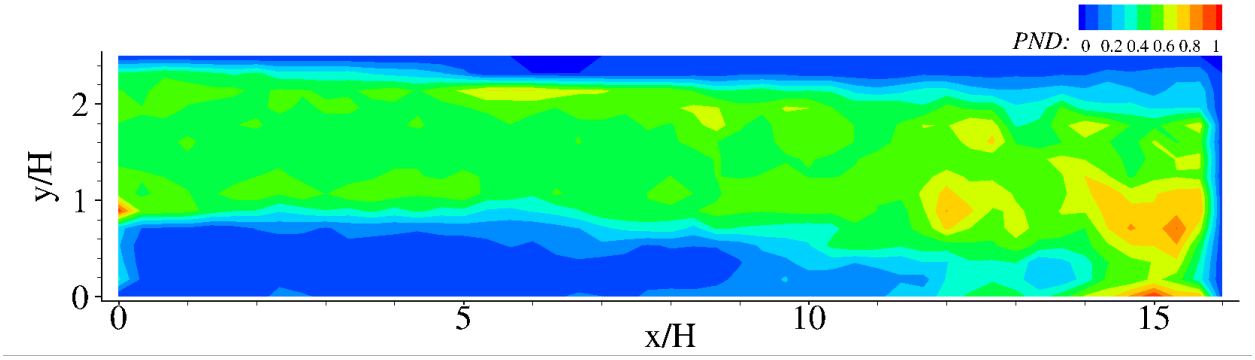

(b) $St = 1$

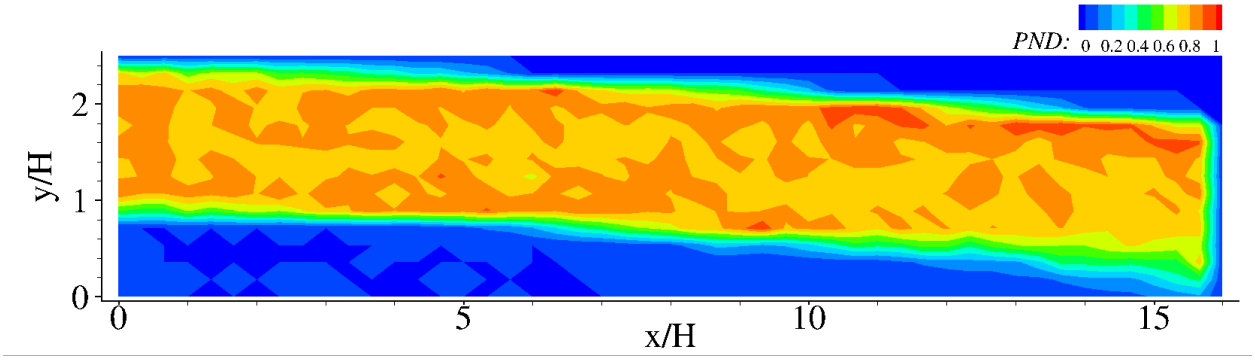

(c) $St = 10$

Figure 6.4 Normalized particle number density contours for the cases with different values of Stokes number in the central $x - y$ plane

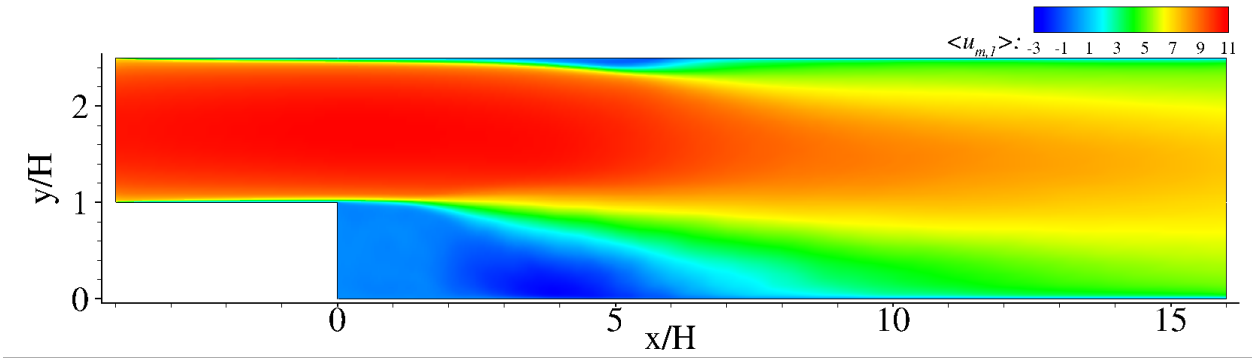

(a) $St = 0.1$

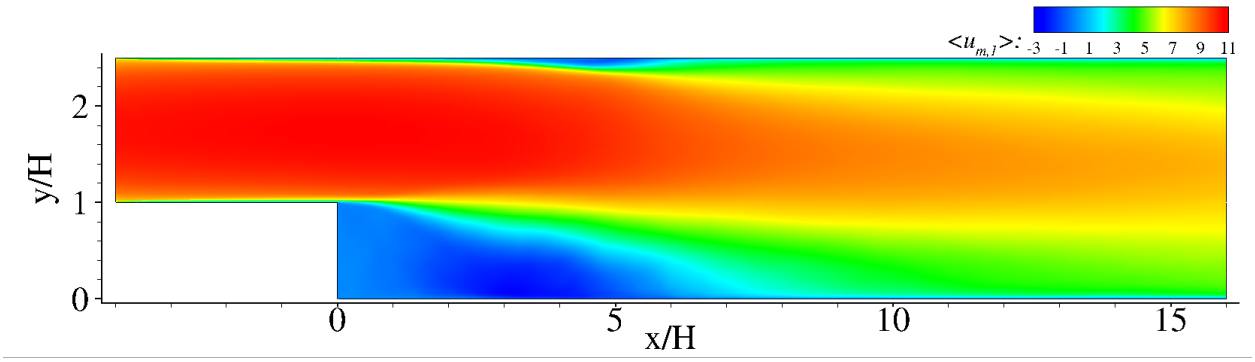

(b) $St = 10$

Figure 6.5 Contours of time-averaged carrier phase streamwise velocity for cases with $St = 0.1$ and 10 in the central $x - y$ plane

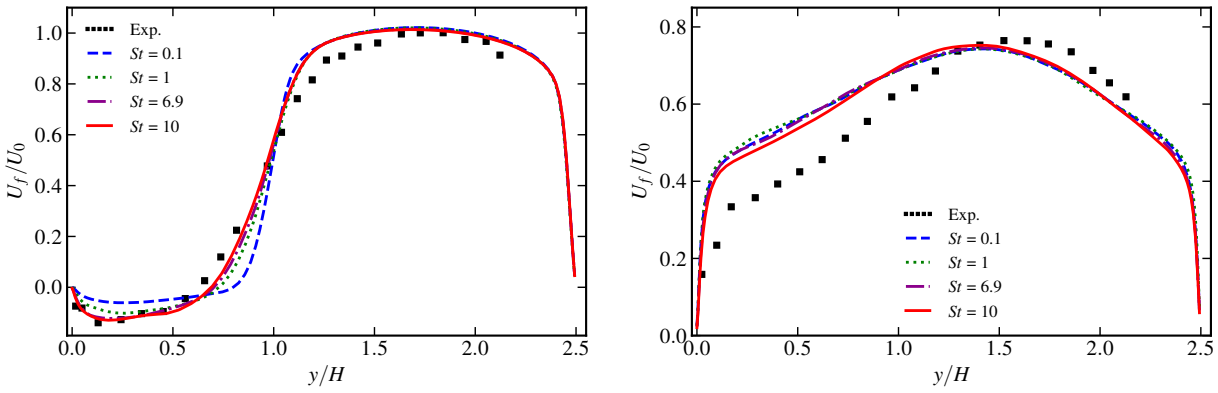

(a) $x/H = 2$ (b) $x/H = 14$

Figure 6.6 Normalized streamwise mean velocity profile at two streamwise locations downstream of the step obtained from different Stokes number cases and compared with the experimental profile

noticeable as well. The spreading of the shear layer in the transverse (y) direction increases with an increase in St, which, in turn, affects the reattachment length x_{R}, of the primary recirculation zone. The value of x_{R} is 6.5, 6.3, 6.3, and 6.1 for cases with $St = 0.1$, 1, 6.9, and 10, where, in general, a decrease in x_{R} occurs with an increase in St. The behavior of $St = 1$ is somewhat different where the particles tend to behave differently compared to tracers or ballistic with respect to the carrier phase flow field.

A further quantitative assessment of the effects of St on the carrier phase statistics is performed in terms of wall-normal variation of the normalized mean streamwise velocity and its intensity. These are shown at two streamwise locations ($x/H = 2$ and $x/H = 14$) downstream of the step in Figs. 6.6 and 6.7, respectively. The increase in St affects the profile of streamwise velocity particularly in the lower half of the channel ($y/H < 1$) at both locations. Note that in this region, we have significant spatio-temporal variations in the carrier phase flow field (see Figs. 6.2 and 6.5), which, in turn, are further affected by

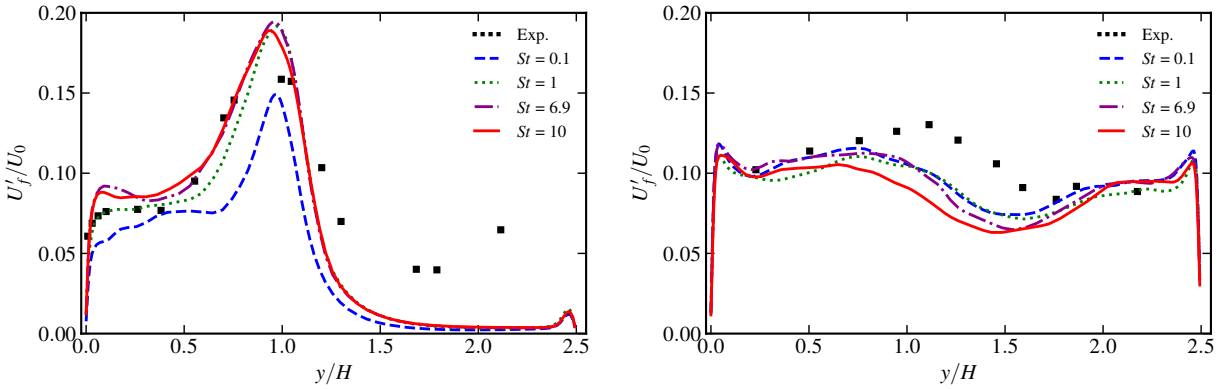

(a) $x/H = 2$ (b) $x/H = 14$

Figure 6.7 Normalized streamwise intensity at two streamwise locations downstream of the step obtained from different Stokes number cases and compared with the experimental profile

the particle-to-fluid coupling effects as particles tend to move toward the lower half of the channel due to gravity. Note that the reference results from experiments correspond to $St = 6.9$. Therefore, the profile from $St = 6.9$ case follows the experimental profile closely compared to the low and the high St cases, particularly at $x/H = 2$ location. A thinner shear layer is present $St = 0.1$ case, which was also observed in Fig. 6.5. In the upper half of the channel ($y/H > 1$), the effects of St on the mean velocity profile tend to decrease indicating that the coupling from the dispersed phase has reduced effects, which is again due to particles moving towards the lower half of the channel due to gravity. The effects of St on the streamwise intensity are much more pronounced at both the locations as evident from Fig. 6.7. Similar to the mean velocity profile, $St = 6.9$ cases tend to follow the reference experimental profile closely compared to low and high St cases, particularly at $x/H = 2$. At the further downstream location, the intensity in the core region of the channel gradually gets smaller with an increase in St.

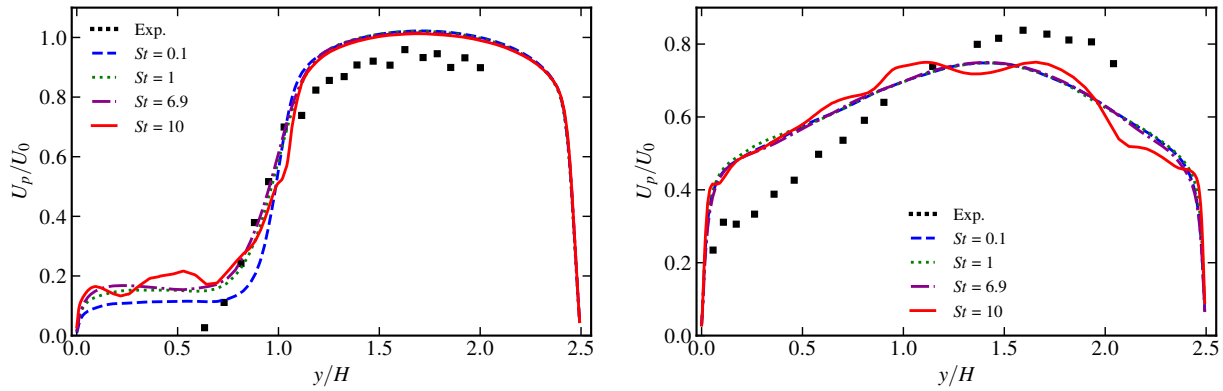

(a) $x/H = 2$ (b) $x/H = 14$

Figure 6.8 Normalized streamwise mean velocity profile of the dispersed phase at two streamwise locations downstream of the step obtained from different Stokes number cases and compared with the experimental profile

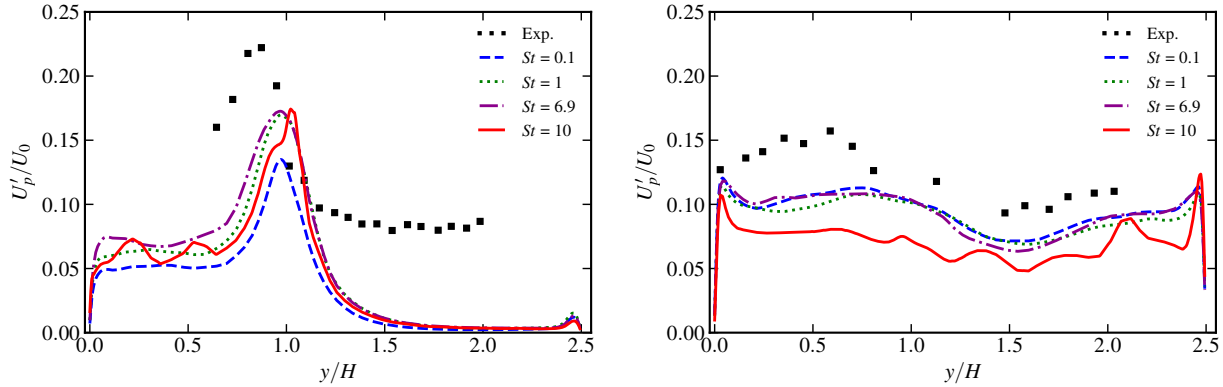

(a) $x/H = 2$ (b) $x/H = 14$

Figure 6.9 Normalized streamwise velocity fluctuations of the dispersed phase at two streamwise locations downstream of the step obtained from different Stokes number cases and compared with the experimental profile

A further assessment is of the dispersed phase mean streamwise velocity and streamwise turbulent intensity at the closest and furthest locations downstream from the step, as shown in Figures 6.8 and 6.9. For the mean velocity at the closest location to the step, the $St = 1$ and 6.9 cases match the experimental profile in the lower half of the channel. For

other locations, the profiles tend to overlap, denoting the Stokes number does not affect the predictions of the mean velocity. This is because the fluctuations are averaged out over time. For the turbulent intensities, the models produce the same behavior, with the higher Stokes numbers producing higher magnitudes, but none match the experimental data well.

Overall, the results presented in this section highlight the role of St on the dynamics and statistics of both the carrier and the dispersed phases. The change in St essentially affects the inertia of particles, which causes a difference in the response of the particles to the local carrier phase variations leading. The modified response by the particles, in turn, feeds back to the evolution of the carrier phase flow field due to the particle-to-fluid coupling effect, which, in turn, is also influenced by the gravity force.

6.3 Effects of Particle-to-Fluid Coupling

The particle-to-fluid coupling becomes important at higher mass loading ($\Phi_{\mathrm{m}} \geq 0.10$) [8]. Here, we examine the role of coupling on the carrier and dispersed phase dynamics and statistics by considering two cases with $\Phi_{\mathrm{m}} = 0.2$ and $St = 1$. These cases differ only in terms of coupling, as the two-way coupling effect is disabled in one of them.

Figure 6.10 compares the instantaneous velocity of the carrier phase overlaid with particles in the central plane from the cases with one-way and two-way coupling effects. Qualitatively, both cases show a similar type of spatial distribution of the particles, where the particles tend to follow the large-scale flow features of the carrier phase flow field. However, the case with the two-way coupling effect shows an increased level of dispersed distribution of particles, especially further downstream in the channel, i.e., for $x/H > 10$. Additionally, the

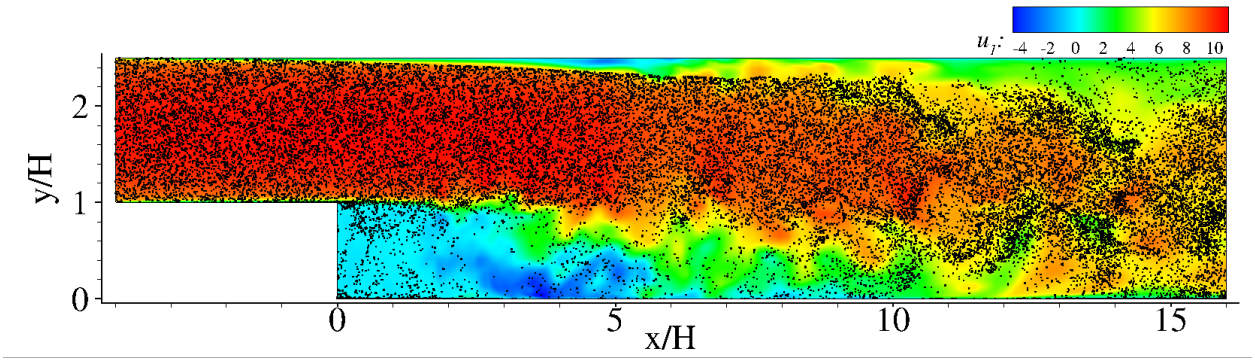

(a) $\Phi_m = 0.20$ - 1W

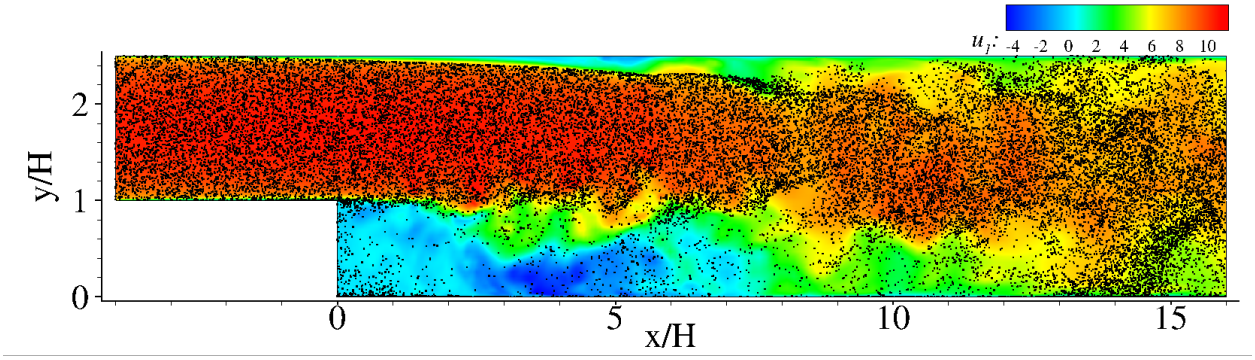

(b) $\Phi_m = 0.20$ - 2W

Figure 6.10 Spatial distribution of particles overlaid on the instantaneous carrier phase streamwise velocity contour for cases with one-way and two-way coupling

shear layer spreading in the transverse direction tends to be higher in the two-way coupled case, which is discussed later in terms of the time-averaged statistics. Further analysis of

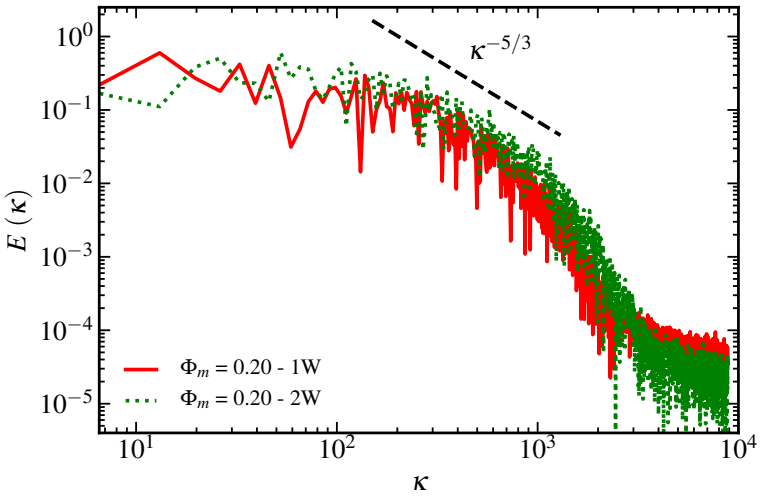

Figure 6.11 Resolved turbulent kinetic energy spectrum from the cases with one-way and two-way coupling at location ($x/H = 2.74,\ y/H = 0.75$) in the central $x - y$ plane

the effects of the two-way coupling on the modulation of the carrier phase turbulent flow field is carried out in terms of the behavior of the resolved turbulent kinetic energy (TKE) spectrum. The spectra of TKE for the two cases at a location within the shear layer region are shown in Fig. 6.11. Both cases show the presence of an inertial range with a $-5/3^{\text{rd}}$ power-law behavior. The effect of coupling is noticeable in the inertial range, where an increase in the resolved TKE occurs across the scales within this range. A substantial noise is observed in the viscous dissipation range, although, the two-way coupled case consistently shows a reduced level of the resolved TKE at such scales.

The particle number density is compared for the one-way and two-way coupled cases in Figure 6.12. The profiles are similar, as the only difference was the two-way coupling

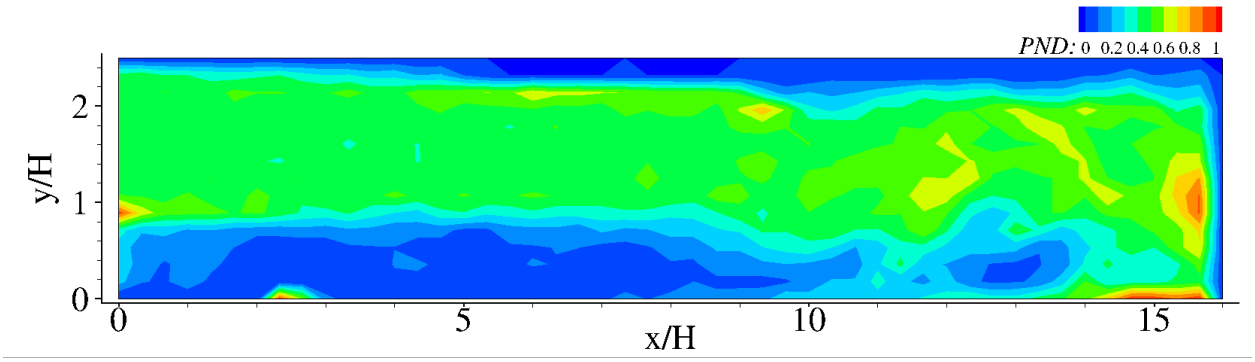

(a) $\Phi_m = 0.20$ - 1W

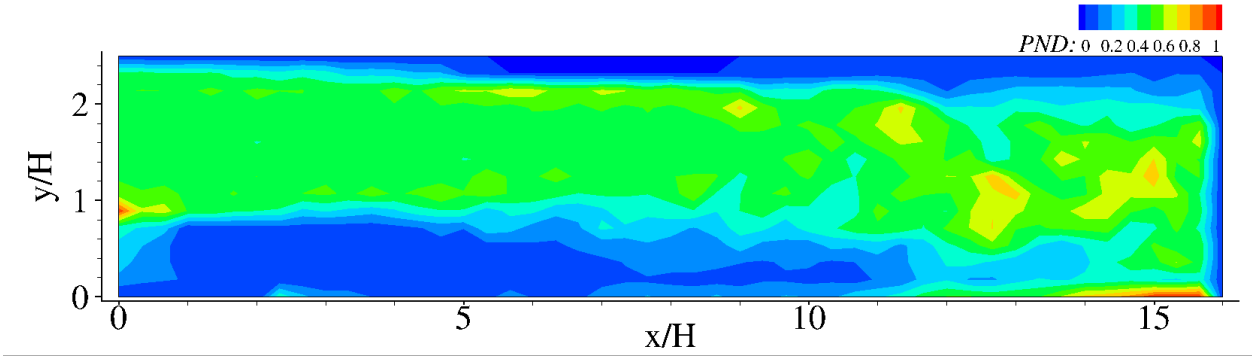

(b) $\Phi_m = 0.20$ - 2W

Figure 6.12 Normalized particle number density contour for the cases with one-way and two-way coupling in the central $x - y$ plane

effects. Still, more small-scale features can be seen in the two-way coupled case due to the increased particle dispersion.

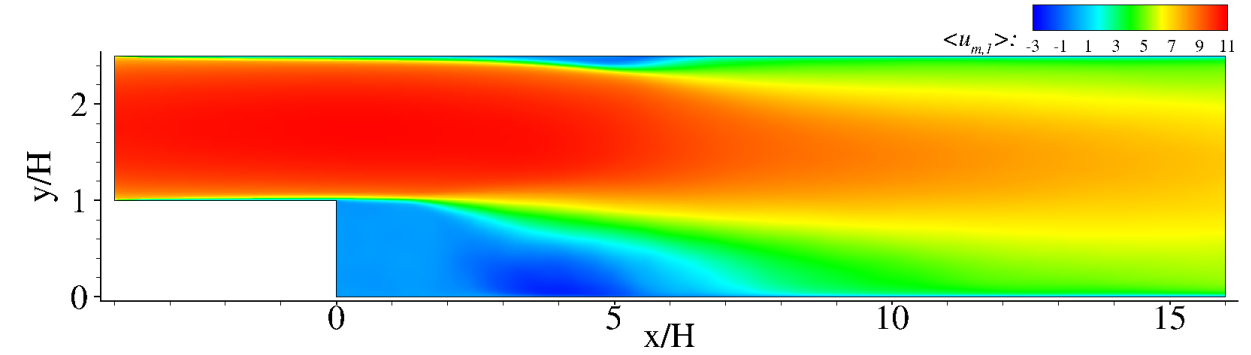

(a) $\Phi_m = 0.20$ - 1W

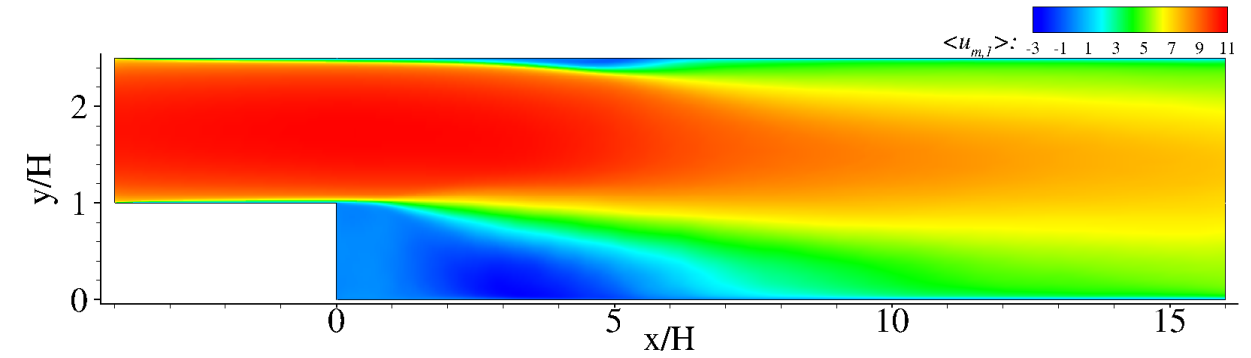

(b) $\Phi_m = 0.20$ - 2W

Figure 6.13 Time-averaged carrier phase streamwise velocity contour for cases with one-way and two-way coupling

Now, we examine the effects of coupling on the time-averaged contours of the streamwise velocity, which are shown in Fig. 6.13 for the two cases. The effects are apparent on the spatial development within the shear layer region. In the two-way coupled case, the spreading of the shear layer is higher at around $x/H \approx 1$, which can be attributed to a relatively higher TKE observed in Fig. 6.11 for a range of scales. However, the reattachment length x_{R} still tends to remain nearly similar in the two cases, which is 6.1 and 6 in the one-way and two-way coupled cases. Further downstream of the reattachment location, qualitatively

the contours of the streamwise velocity field tend to be similar indicating minimal effects of the two-way coupling in these regions. This is also evident from the wall-normal profiles of the time-averaged streamwise velocity profile at two different locations, which are shown in Fig. 6.14. At $x/H = 2$, the two-way coupled case shows a thicker shear layer compared to the one-way coupled case. The differences though between these cases are negligible at $x/H = 14$. Such a behavior can be attributed to the role of gravity as most of the particles tend to settle close to the lower wall further downstream in the channel, thus leading to a reduced feedback effect from the dispersed phase to the carrier phase flow field in the regions away from the wall. The case with two-way coupling effects also produces a higher turbulent intensity of the carrier phase at $x/H = 2$, as shown in Figure 6.15 (a). The differences between the two cases are not substantial further downstream.

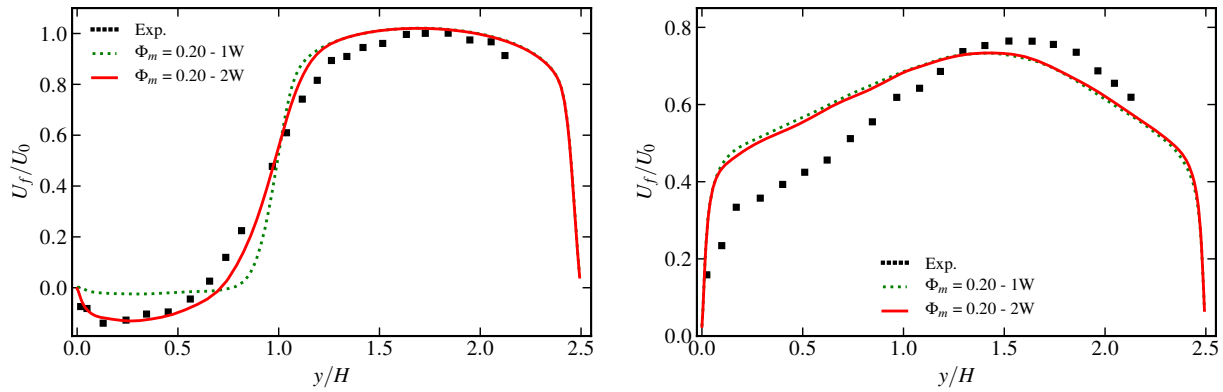

(a) $x/H = 2$ (b) $x/H = 14$

Figure 6.14 Normalized streamwise mean velocity profile of the carrier phase at two streamwise locations downstream of the step obtained from cases with one-way and two-way coupling and compared with the experimental profile

The particle-to-fluid coupling also affects the statistics of the dispersed phase. This is shown in terms of the wall-normal profile of the normalized time-averaged streamwise mean

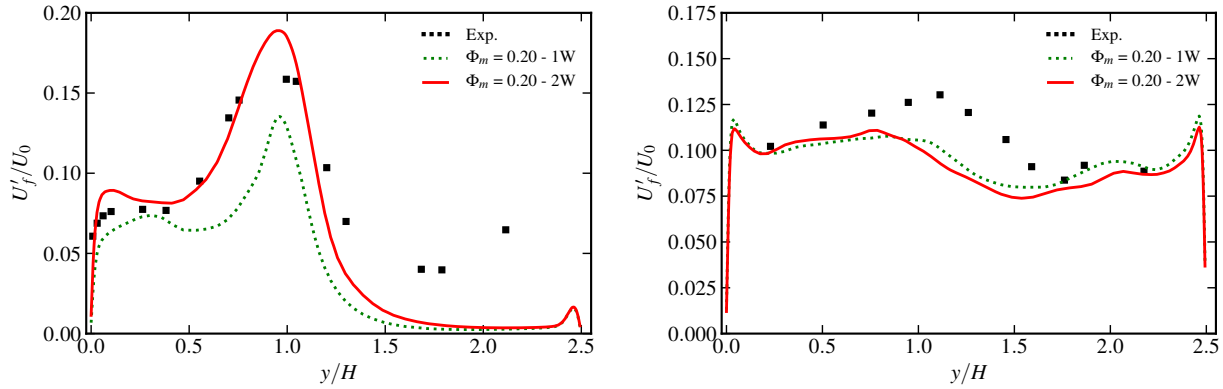

(a) $x/H = 2$ (b) $x/H = 14$

Figure 6.15 Normalized streamwise intensity at two streamwise locations downstream of the step obtained from cases with one-way and two-way coupling and compared with the experimental profile

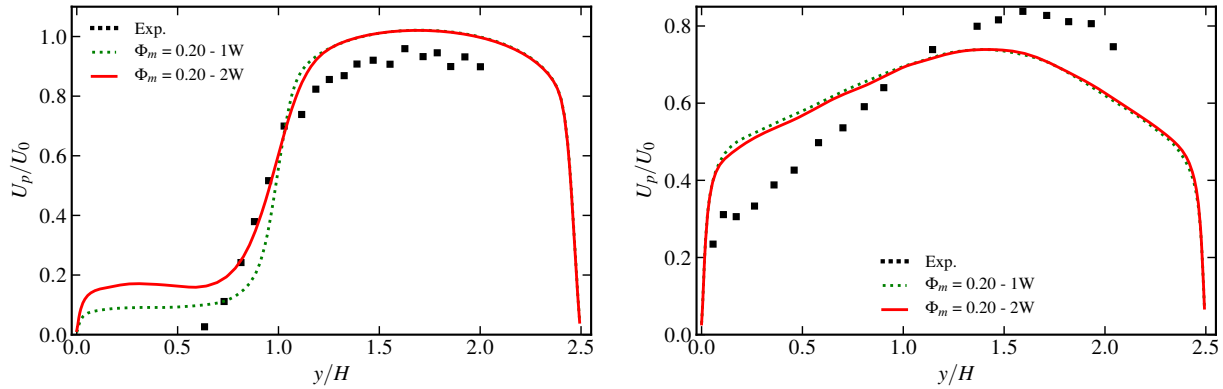

(a) $x/H = 2$ (b) $x/H = 14$

Figure 6.16 Normalized streamwise mean velocity profile of the dispersed phase at two streamwise locations downstream of the step obtained from cases with one-way and two-way coupling and compared with the experimental profile

particle velocity and turbulent intensity shown in Figs. 6.16 and 6.17 at two streamwise locations. For the mean velocity, as expected, the case with the two-way coupling enabled closely follows the experimental profile at $x/H = 2$ particularly in the lower half of the channel. Similar to the carrier phase, the case with the one-way coupling shows a sharper

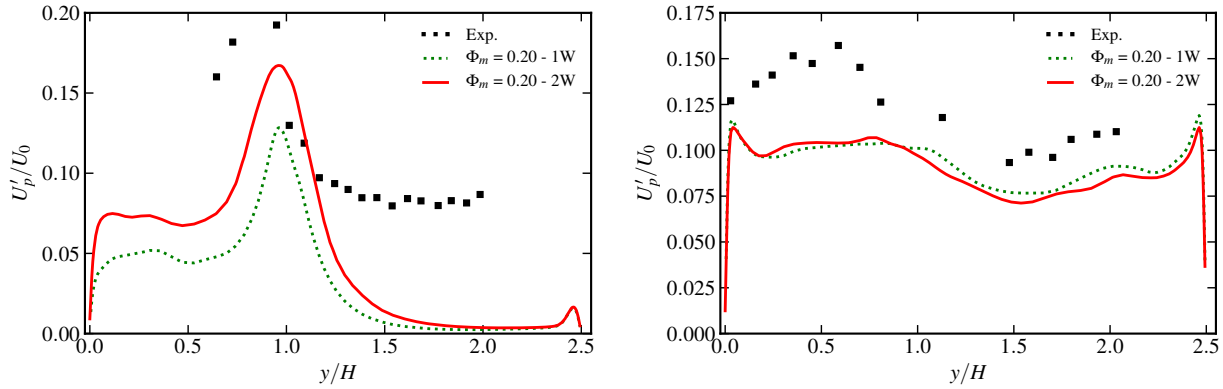

(a) $x/H = 2$ (b) $x/H = 14$

Figure 6.17 Normalized streamwise velocity fluctuations of the dispersed phase at two streamwise locations downstream of the step obtained from cases with one-way and two-way coupling and compared with the experimental profile

variation within the shear layer region and shows a lower velocity near the bottom wall compared to the two-way coupled case. The turbulent fluctuations are also closer to the experimental data for the two-way coupled case at $x/H = 2$, yet still much lower in the upper part of the channel. This can be contributed to the Stokes number of these cases, as the experimental data was obtained for $St = 6.9$ Away from the shear-layer region at $x/H = 2$ and further downstream location, i.e., $x/H = 14$, both cases show a similar variation for the mean velocity and turbulent intensity, thus indicating negligible effects of coupling.

The results presented in this section demonstrate the role of two-way coupling on the evolution of both carrier and dispersed phases. The effects are important particularly in the shear-layer and separated flow regions, which affect the instantaneous, spectral, and statistical features of the flow field. This is mainly due to modulation of the turbulence by the particles when the two-way coupling effects are enabled, which can attenuate or enhance

the TKE depending upon the scales of the flow field. The two-way coupling, therefore, affects the inter-scale interactions in the carrier phase, which in turn can affect the evolution of the inertial particles.

6.4 Effects of Polydispersity

Since real-world applications have variability in particle dimensions, a distribution of particle sizes is natural. This not only provides a larger distribution of energy scales for the dispersed phase but also provides different inertial responses. In the E-L point-particle-based approach, although the physical size of particles is not explicitly accounted for, the particle relaxation time implicitly accounts for the effects of particle sizes [12]. To examine the effects of variability in particle sizes while considering inertial particles, we assess two different types of distribution by comparing with the results from a mono-disperse distribution of particles with $St = 1$ and $\Phi_{\mathrm{m}} = 0.2$. In the polydisperse cases, the lower and upper bounds for the diameter of particles are specified to be $d_{\mathrm{min}}/d_{\mathrm{m}} = 0.85$, and $d_{\mathrm{max}}/d_{\mathrm{m}} = 1.15$, respectively. We employ two distributions, namely a uniform distribution and a Gaussian distribution, with the standard deviation of particle diameter specified as $\sigma/d_{\mathrm{m}} = 0.09$.

The contours of the instantaneous velocity of the carrier phase, overlaid with the spatial distribution of particles, are shown for the three types of particle size-distributions in Fig. 6.18. Qualitatively, all the cases show a similar spatial distribution of particles up to $x/H = 10$, where most of the particles tend to concentrate in the core region of the channel with effects of gravity also noticeable. However, further downstream, qualitative differences in the distribution of particles are noticeable, where the cases with mono-disperse

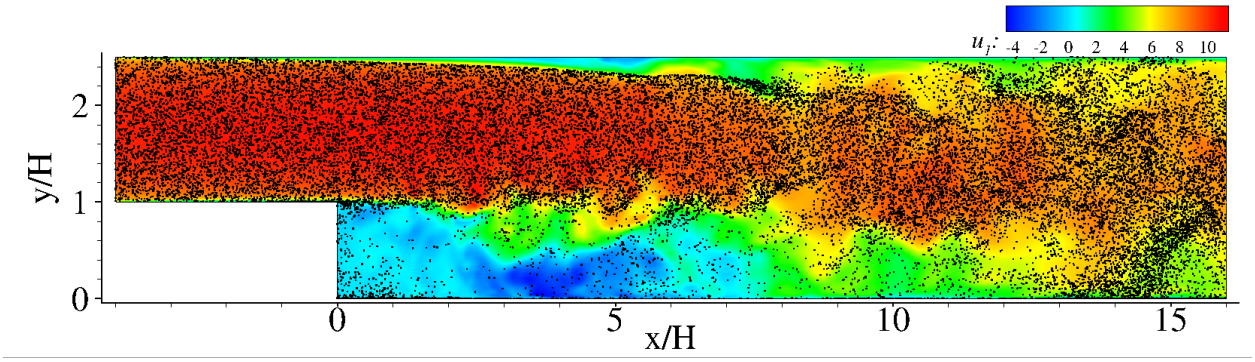

(a) Mono-disperse

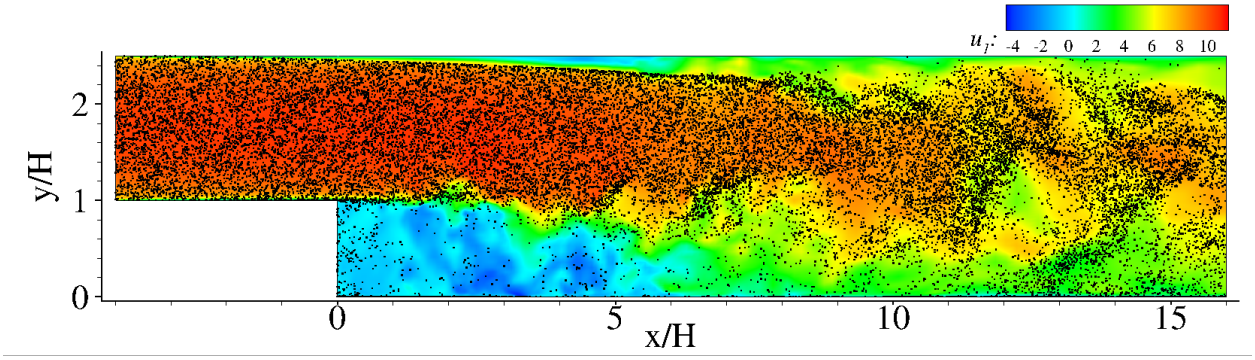

(b) Uniform distribution

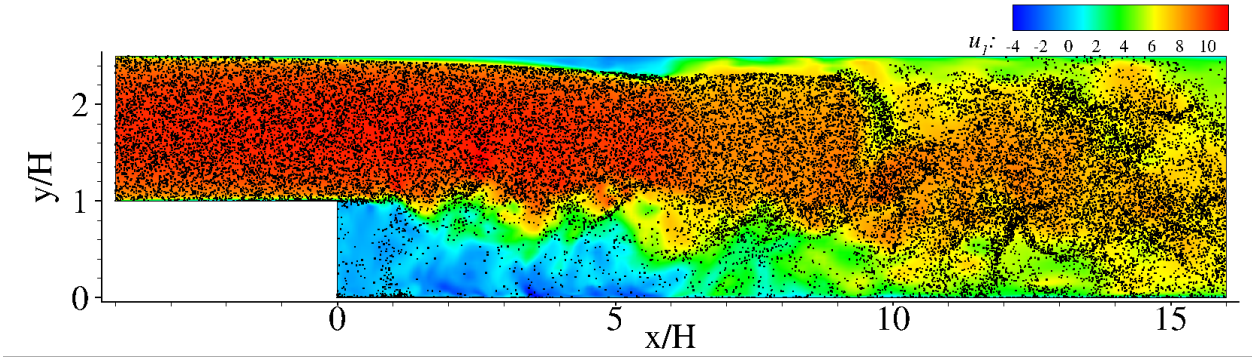

(c) Gaussian distribution

Figure 6.18 Particle distribution overlaid on the instantaneous carrier phase streamwise velocity contour for cases with different types of distribution of particles

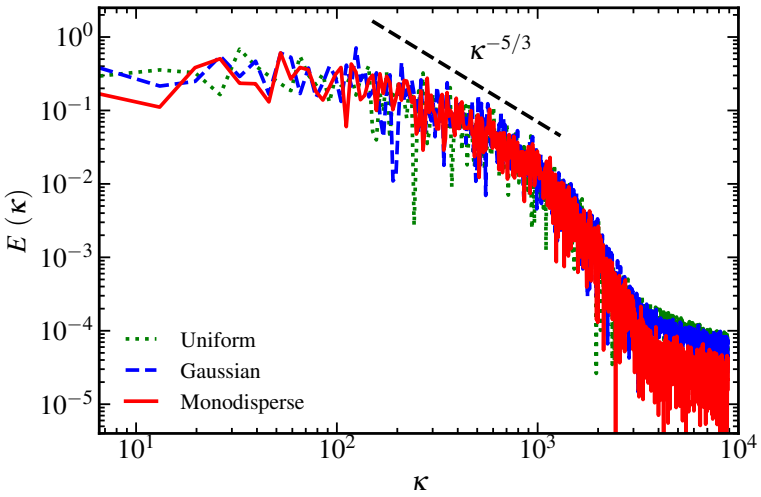

Figure 6.19 Resolved turbulent kinetic energy spectrum in the shear layer ($x/H = 2.74$, $y/H = 0.75$) for the case with different types of particle distributions

and Gaussian distributions show a similar dispersion of particles compared to the case using a uniform distribution of particles.

Figure 6.19 compares the resolved TKE spectra obtained from mono-disperse and poly-disperse cases. All the cases show the $-5/3^{\text{rd}}$ power-law behavior in the inertial range. However, the polydisperse cases exhibit higher variability in the inertial range, thus indicating enhanced fluctuations in the flow field due to particles with different levels of inertia. The TKE corresponding to the small-scale viscous dissipation range is also higher in the polydisperse case compared to the mono-disperse case, with the case employing uniform distribution showing a consistently higher level of TKE corresponding to small-scales. Although the first and second-order statistics of the employed distributions for the polydispersed cases are the same, the intermittency of the particle sizes in the case with the uniform distribution is large, thus enhancing the level of intermittency of the coupling effects from the dispersed phase to the carrier phase.

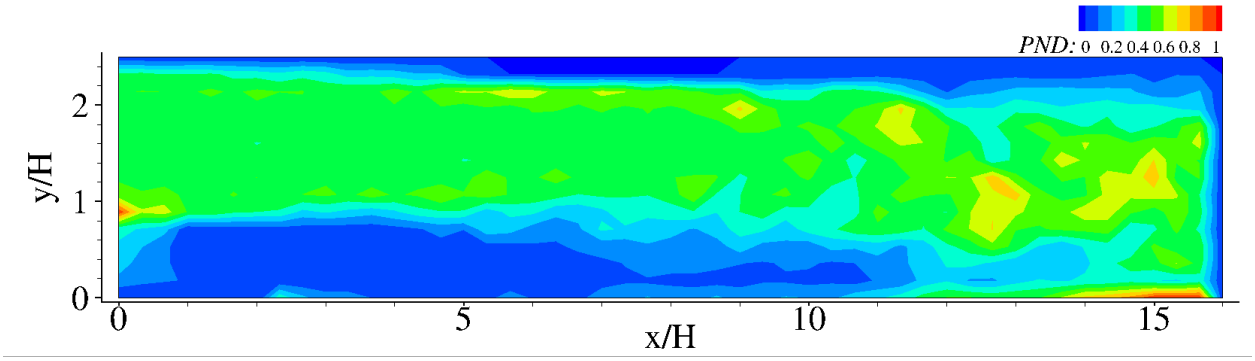

(a) Mono-disperse

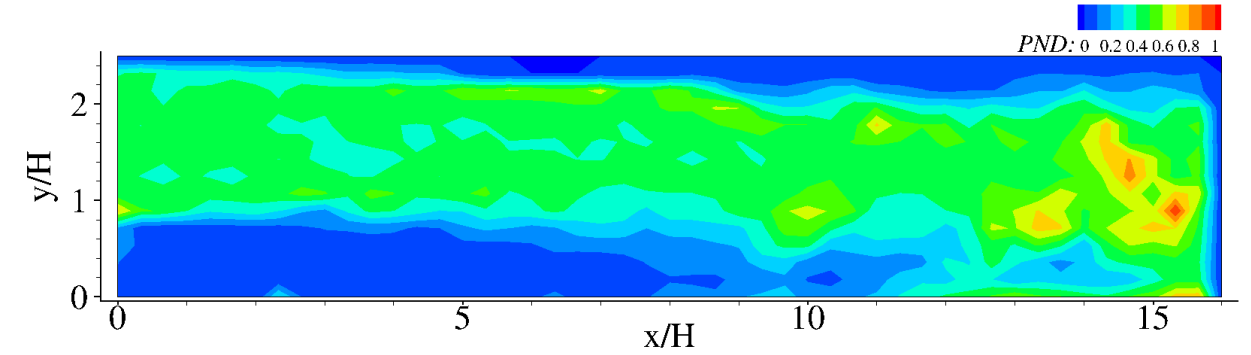

(b) Gaussian distribution

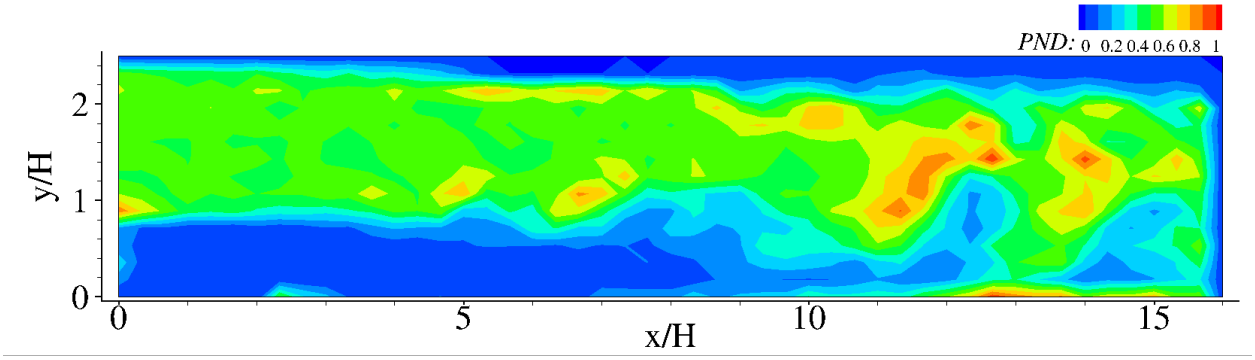

(c) Uniform distribution

Figure 6.20 Normalized particle number density contour for the cases with different types of particle distributions in the central $x - y$ plane

Figure 6.20 compares the normalized particle number density contours for the different particle size distributions considered here. Both poly-disperse cases display more intermittency of the number density throughout the channel, with the uniform distribution displaying more of these features. The mono-disperse and Gaussian distributions are the most similar.

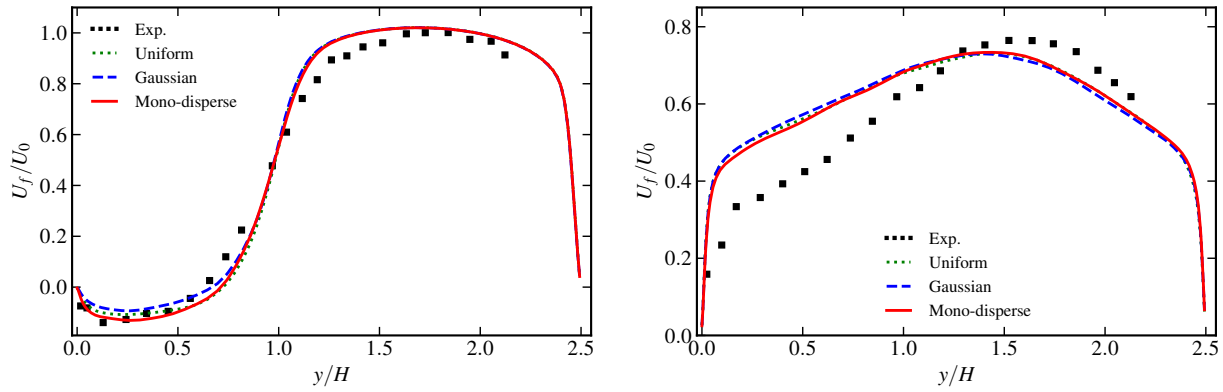

(a) $x/H = 2$ (b) $x/H = 14$

Figure 6.21 Normalized streamwise mean velocity profile of the carrier phase at two streamwise locations downstream of the step obtained from the cases employing mono- and poly-disperse distributions of particle size and compared with the experimental profile

Qualitatively, the time-averaged contours of the streamwise velocity of the carrier phase in the central plane are nearly identical in the three cases considered here and therefore are not shown here for brevity. This is also evident from the wall-normal profile of the streamwise velocity at $x/H = 2$ and 14 in Fig. 6.21, where we can observe nearly overlapping profiles from the three cases. This is also true for the streamwise turbulent intensity profiles, shown in Figure 6.22, with the polydisperse cases only providing a slight increase in the intensity. The mean reattachment length, although, shows some variability, where $x_{\mathrm{R}} = 6$,

5.9, 6.2 from the mono-disperse, Gaussian distribution, and uniform distribution cases. Such a variation can be attributed to the nonlinear effects of coupling and intermittency in the size distribution of particles, which, in turn, can modulate the turbulent flow field.

Similar to the time-averaged statistics of the carrier phase, the wall-normal profiles of the streamwise particle velocity and turbulent intensity fields shown in Figs. 6.23 and 6.24 do not show any significant effects of polydispersity. The profiles at both of the streamwise locations tend to nearly collapse. The results presented in this section demonstrate that the

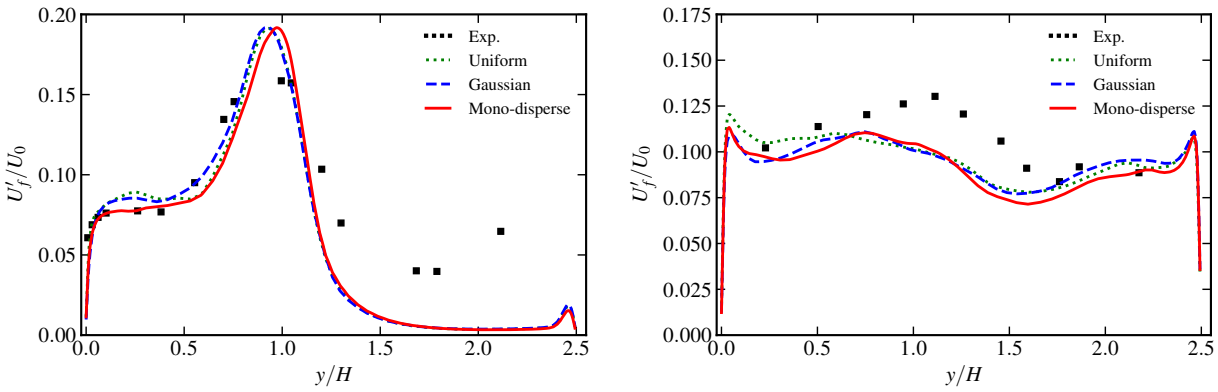

(a) $x/H = 2$ (b) $x/H = 14$

Figure 6.22 Normalized streamwise intensity at two streamwise locations downstream of the step obtained from cases with the cases employing mono- and poly-disperse distributions of particle size and compared with the experimental profile

effects of polydispersed distribution are mainly on the instantaneous and spectral features of the carrier and the dispersed phases. However, the effects of polydispersity on the first-order time-averaged statistics of the carrier and dispersed phases tend to be negligible, at least for the considered level of variations in the diameter of the particles.

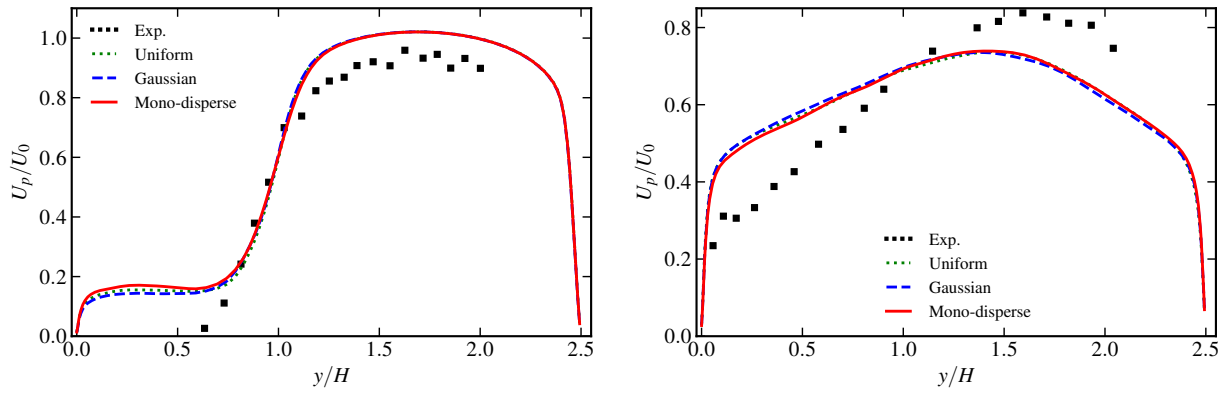

(a) $x/H = 2$ (b) $x/H = 14$

Figure 6.23 Normalized streamwise mean velocity profile of the dispersed phase at two streamwise locations downstream of the step obtained from the cases employing mono- and poly-disperse distributions of particle size and compared with the experimental profile

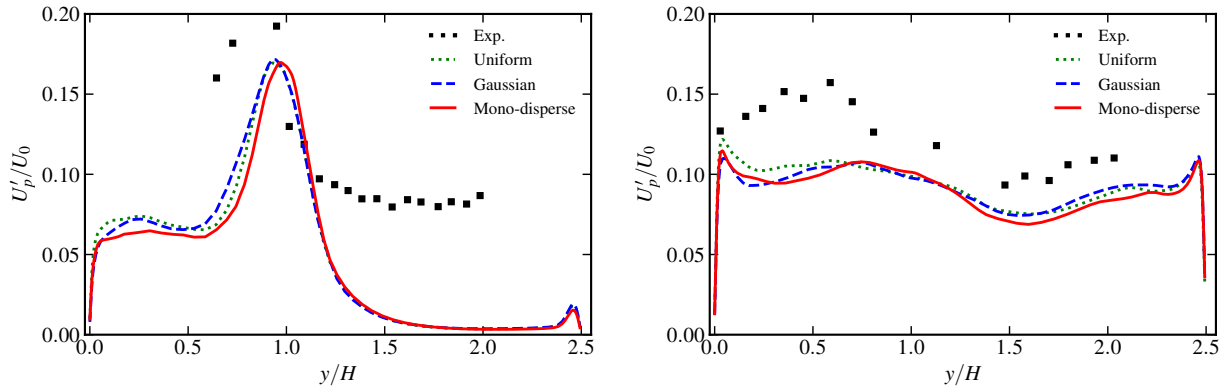

(a) $x/H = 2$ (b) $x/H = 14$

Figure 6.24 Normalized streamwise velocity fluctuations of the dispersed phase at two streamwise locations downstream of the step obtained from the cases employing mono- and poly-disperse distributions of particle size and compared with the experimental profile

CHAPTER 7

CONCLUSIONS

The point-particle-based strategy for large-eddy simulation (LES) while considering the Eulerian-Lagrangian method is a computationally tractable approach for numerical investigation of particle-laden turbulent flows that are observed in engineering and natural systems. The present study focused on two aspects of LES-based studies of such flows. The first focus was on assessing the performance of the well-established subgrid models for the closure of the subgrid-scale (SGS) stress tensor and the subgrid dispersion. The emphasis of the second part of the study was to examine the effects of parameters that govern the physical processes in these flows. The study has been performed by considering the widely studied test configuration, referred to as turbulent flow over a backward-facing step at $Re_{\mathrm{H}} = 18,400$. This model configuration is commonly observed in many engineering applications and allows for the study of complex physical phenomena in a geometrically simpler setup. The computational setup primarily focused on a two-way coupled configuration for which reference results were available in the literature. The simulations were carried out using an in-house extended version of the OpenFOAM software. In the following sections, first, the key accomplishments of this study are described. Afterward, potential future studies that can be carried out based on this study are discussed.

7.1 Key Accomplishments

The key accomplishments of this study are as summarized as follows:

- **Subgrid model implementation in OpenFOAM**: The focus of the study on the assessment of the subgrid models was to consider three well-established eddy viscosity based closures, namely, WALE, DEVM, and LDKM for the closure of the SGS stress tensor, and RW and DF models for the subgrid dispersion. The open-source version of OpenFOAM software considered here had WALE and LDKM options available. It had no options for the DEVM and the subgrid dispersion. Therefore, the solver was extended to include these models for assessment studies.

- **Assess closures for SGS stress tensor term:** The unladen configuration was considered to examine the performance of WALE, DEVM, and LDKM modeling strategies while employing a coarse grid computational setup. An additional simulation employing a no-model strategy was also considered to demonstrate the need for SGS closure. The assessment was performed in terms of comparison of metrics, which include the first- and second-order statistics of the flow field (wall-normal profile of streamwise velocity at different streamwise locations) and the mean reattachment length with respect to the experimental results. The analysis of results showed that the no-model strategy yields inaccurate results and both WALE and LDKM showed overall a good agreement with experiments. The quality of agreement with the experimental data was better in the regions closer to the vicinity of the step. As the cost of the algebraic WALE model is 37% lower than the one-equation-based LDKM, therefore, WALE model was

considered for further studies.

- **Grid Convergence Study**: The unladen setup was chosen to carry out a grid convergence study where the WALE model was used for the closure of the SGS stress tensor. For this, three grids labeled as coarse, medium, and fine with 0.26 M, 0.92 M, and 2.18 M cells, respectively, were considered. As the grid was refined all the metrics showed an improvement agreement with the experimental results. However, the improvement was much more apparent as the grid was refined from coarse to medium and nominal from medium to fine. To keep further computations in this study tractable and leverage the benefits of subgrid modeling, the medium grid was chosen for further studies.

- **Assess closures for subgrid dispersion:** We considered the two-way coupled particle-laden flow with $St = 6.9$ and $\Phi_{\mathrm{m}} = 0.1$ to examine the performance of RW, DF, and no-model approaches for the closure of subgrid dispersion using the fine mesh setup. Overall, the performance of the stochastic RW model has been proven to work best in terms of metrics for reattachment length and the fluctuating particle velocity in the core region of the channel. The other statistics were less sensitive to the type of the employed subgrid dispersion model.

- **Application studies:** A major focus of the study was to use the optimal subgrid models to perform LES-based investigation of the effects of particles inertia, coupling, and a polydisperse distribution of the particles. The effects of inertia of particles were examined by simulating 4 cases with St of 0.1, 1, 6.9, and 10. To study the effects of two-way coupling, two cases at $St = 1$ were considered, where they differ in terms

of feedback from particles to the fluid. Overall, the dynamics, spectral characteristics, and the statistics of the carrier and the dispersed phases were observed to be sensitive to the effects of inertia of particles as well as two-way coupling. However, for the considered level of the polydispersity, where the results from the uniform and Gaussian distributions were compared with the mono-disperse case, the sensitivity of the results was smaller, although variations were observed in the spectrum of the resolved turbulent kinetic energy.

7.2 Future Outlook

The goal of the present study was to assess the performance of subgrid models for LES of two-way coupled particle-laden turbulent flow in a canonical separating/reattaching flow to enable cost-efficient LES of such flows for parametric studies. The present study can be extended in several directions to accomplish different goals. Some of these directions are summarized below:

- **Model improvements**: To enhance the predictive capabilities of the subgrid dispersion models, there is a need to extend their regime of applicability. Some specific future work can focus on the use of a dynamic procedure to determine the model parameters in the DF model for non-homogeneous wall-bounded flows. Furthermore, a hybrid stochastic/deconvolution-based strategy or, a multi-scale approach can be considered for modeling subgrid dispersion.

- **Improved point-particle strategy**: Although particle-resolved LES still tends to be intractable for applications, however, the underlying mathematical model for point-

particle LES can be improved by accounting for the effects of finite-size particles on the carrier phase, particularly, in a two-way coupled scenario. Therefore, canonical configurations with a limited number of particles can be considered to perform particle-resolved simulations for improvements of subgrid models to be used in the point-particle-based strategy.

- **Extend the analysis to reacting cases:** Since many combustion processes such as engines or furnaces use spray injection of fuels, therefore, the present study can be considered for such configurations. This will require additional models to account for subgrid fluctuations in the temperature field of the carrier phase and handling of evaporation of particles where the size of particles changes. The wide range of complex phenomena involved in such cases requires a systematic study of different physical processes to understand the role of subgrid quantities on the resolved quantities while performing LES.

REFERENCES

[1] S. Elghobashi, On predicting particle-laden turbulent flows, Applied Scientific Research 52 (1994) 309–329.

[2] G. Jin, G.-W. He, L.-P. Wang, Large-eddy simulation of turbulent collision of heavy particles in isotropic turbulence, Physics of Fluids 22 (2010) 055106.

[3] D. Rouson, J. Eaton, On the preferential concentration of solid particles in turbulent channel flow, J. Fluid Mech. 428 (2000) 149–169.

[4] M. Bini, W. Jones, Large-eddy simulation of particle-laden turbulent flows, J. Fluid Mech. 614 (2008) 207–252.

[5] V. Mathai, D. Lohse, C. Sun, Bubbly and Buoyant Particle-Laden Turbulent Flows, Annu. Rev. Condens. Matter Phys. 11 (2020) 529–559.

[6] J. B. de Motta, P. Costa, J. Derksen, C. Peng, L.-P. Wang, J. L. Estivalezes, S. Vincent, E. Climent, P. F. amd P. Barbaresco, N. Renon, Assessment of numerical methods for fully resolved simulations of particle-laden turbulent flows, Comput. Fluids 179 (2019) 1–14.

[7] J. Fessler, J. Eaton, Turbulence modification by particles in a backward-facing step flow, J. Fluid Mech. 394 (1999) 97–117.

[8] S. Balachandar, J. Eaton, Turbulent Dispersed Multiphase Flow, Annu. Rev. Fluid Mech. 42 (2010) 111–133.

[9] C. Tu, Z. Yin, J. Lin, F. Bao, A Review of Experimental Techniques for Measuring Micro- to Nano- Particle-Laden Gas Flows, Appl. Sci. 7 (2017) 1–21.

[10] S. Menon, P.-K. Yeung, W.-W. Kim, Effect of Subgrid Models on the Computed Interscale Energy Transfer in Isotropic Turbulence, Computers and Fluids 25 (1995) 165–180.

[11] G. Park, M. Bassenne, J. Urzay, P. Moin, A simple dynamic subgrid-scale model for LES of particle-laden turbulence, Phys. Rev. Fluids 2 (2017) 044301.

[12] J. Kuerten, Point-particle DNS and LES of particle-laden flow - a state-of-the-art review, Flow Turbulence Combust. 97 (2016) 689–713.

[13] C. Marchioli, Large-eddy simulation of turbulent dispersed flows: a review of modelling approaches, Acta Mech. 228 (2017) 741–771.

[14] Z. Wang, H. Wang, K. Luo, J. Fan, Direct numerical saimulation of particle-laden turbulent boundary layers with and without combustion, Physics of Fluids 32 (2020) 105108.

[15] M. Alletto, M. Breuer, One-way, two-way and four-way coupled LES predictions of a particle-laden turbulent flow at high mass loading downstream of a confined bluff body, Int. J. Multiph. Flow 45 (2012) 70–90.

[16] A. Gosman, E. Loannides, Aspects of computer simulation of liquid-fueled combustors, J. Energy 7 (1983) 482–490.

[17] Q. Wang, K. D. Squires, Large eddy simulation of particle-laden turbulent channel flow, Physics of Fluids 8 (1996) 1207–1223.

[18] B. Shotorban, F. Mashayek, A stochastic model for particle motion in large-eddy simulation, J. Turbul. (2006) N18.

[19] A. Berrouk, D. Laurence, J. Riley, D. Stock, Stochastic modelling of inertial particle dispersion by subgrid motion for LES of high Reynolds number pipe flow, J. Turbul. (2007) N50.

[20] M. Bini, W. Jones, Particle acceleration in turbulent flows: A class of nonlinear stochastic models for intermittency, Physics of Fluids 19 (2007) 035104.

[21] J. Pozorski, S. Apte, Filtered particle tracking in isotropic turbulence and stochastic modeling of subgrid-scale dispersion, Int. J. of Multiphase Flow 35 (2009) 118–128.

[22] J.-P. Minier, On Lagrangian stochastic methods for turbulent polydisperse two-phase reactive flows, Prog. Energy Combust. Sci. 50 (2015) 1–62.

[23] B. Shotorban, F. Mashayek, Modeling subgrid-scale effects on particles by approximate deconvolution, Physics of Fluids 17 (2005) 081701.

[24] J. Kuerten, Subgrid modeling in particle-laden channel flow, Physics of Fluids 18 (2006) 025108.

[25] Q. Wang, X. Zhao, M. Ihme, A regularized deconvolution model for sub-grid dispersion in large eddy simulation of turbulent spray flames, Combust. Flame 207 (2019) 89–100.

[26] W. Michalek, J. Kuerten, J. Zeegers, R. Liew, J. Pozorski, B. Geurts, A hybrid stochastic-deconvolution model for large-eddy simulation of particle-laden flow, Physics of Fluids 25 (2013) 123302.

[27] C. Gobert, M. Manhart, Subgrid modelling for particle-LES by Spectrally Optimised Interpolation (SOI), J. Comput. Phys. 230 (2011) 7796–7820.

[28] B. Ray, L. R. Collins, A subgrid model for clustering of high-inertia particles in large-eddy simulations of turbulence, J. Turbul. 15 (2014) 366–385.

[29] S. Murray, M. Lightstone, S. Tullis, Single-particle lagrangian and structure statistics in kinematically simulated particle-laden turbulent flows, Physics of Fluids 28 (2016) 033302.

[30] M. Gorokhovski, R. Zamansky, Lagranigan simulation of large and small inertial particles in a high Reynolds number flow: Stochastic simulation of subgrid turbulence/particle interactions, in: Proceedings of the Summer Program 2014, Stanford, 2014, pp. 37–46.

[31] F. Nicoud, F. Ducros, Subgrid-Scale Stress Modelling Based on the Square of the Velocity Gradient Tensor, Flow Turbulence Combust. 62 (1999) 183–200.

[32] A. Berrouk, D. Laurence, J. Riley, D. Stock, Stochastic modeling of fluid velocity seen by heavy particles for two-phase LES of non-homogeneous and anisotropic turbulent flows, in: Particle-Laden Flow, Springer Netherlands, 2007, pp. 179–192.

[33] H. Jin, Y. Chen, J. Fan, K. Luo, LES/FDF simulation of a gas-particle backward-facing step flow, Chem. Eng. Sci. 66 (2011) 3692–3700.

[34] A. Kartushinsky, S. Tisler, J. Oliveira, C. van der Geld, Eulerian-Eulerian modelling of particle-laden two-phase flow, Powder Technol. 301 (2016) 999–1007.

[35] M. Baker, B. Kong, J. Capecelatro, O. Desjardins, R. Fox, Direct comparison of Eulerian-Eulerian and Eulerian-Lagrangian simulations for particle-laden vertical channel flow, AIChE Journal 66 (2020).

[36] E. S. Vasquez, K. B. Walters, D. K. Walters, Analysis of Particle Transport and Deposition of Micron-Sized Particles in a 90^o Bend Using a Two-Fluid Eulerian-Eulerian Approach, Aerosol Science and Technology 49 (2015) 692–704.

[37] J. Harting, S. Frijters, M. Ramaioli, M. Robinson, D. Wolf, S. Luding, Recent advances in the simulation of particle-laden flows, Eur. Phys. J. Spec. Top. 223 (2014) 2253–2267.

[38] G. Colenbrander, CFD in research for the petrochemical industry, in: Computational Fluid Dynamics for the Petrochemical Process Industry, Springer Netherlands, 1991, pp. 211–245.

[39] J. D. Kulick, J. R. Fessler, J. K. Eaton, Particle response and turbulence modification in fully developed channel flow, J. Fluid Mech. 277 (1994) 109–134.

[40] C. J. Park, L.-D. Chen, Experimental Investigation of Confined Turbulent Jets Part II: Particle-Laden Flow Data, AIAA J. 27 (1989) 1511–1516.

[41] C. Schram, P. Rambaud, M. L. Riethmuller, Wavelet based eddy structure eduction from a backward facing step flow investigated using particle image velocimetry, Exp. in Fluids 36 (2004) 233–245.

[42] J. Kostas, J. Soria, M. Chong, Particle image velocimetry measurements of a backward-facing step flow, Exp. in Fluids 33 (2002) 838–853.

[43] C. E. Tinney, L. S. Ukeiley, A study of a 3-D double backward-facing step, Exp. in Fluids 47 (2009) 427–438.

[44] D. McAndrew, S. Coppen, C. B. Rogers, Measurement of fluid turbulence along the path of a heavy particle in a backward-facing step flow, Int. J. Multiph. Flow 27 (2001) 1517–1532.

[45] L.-X. Zhou, Y. Liu, Y. Xu, Measurement and simulation of the two-phase velocity correlation in sudden-expansion gas-particle flows, Acta Mech. Sin. 27 (2011) 494–501.

[46] U. Piomelli, Large-eddy simulation: Achievements and challenges, Progress in Aerospace Sciences 35 (1999) 335–362.

[47] P. Sagaut, Large eddy simulation for incompressible flows: an introduction, Springer Science & Business Media, 2006.

[48] J. Smagorinsky, General circulation experiments with the primitive equations, Monthly Weather Review 91 (1963) 99–164.

[49] W.-W. Kim, S. Menon, An unsteady incompressible Navier-Stokes solver for large-eddy simulation of turbulent flows, International Journal of Numerical Fluid Mechanics 31 (1999) 983–1017.

[50] M. Germano, U. Piomelli, P. Moin, W. H. Cabot, A dynamic subgrid-scale eddy viscosity model, Physics of Fluids A 3 (1991) 1760–1765.

[51] S. Ghosal, Mathematical and physical constraints on large eddy simulation of turbulence, AIAA Journal 37 (1999) 425–433.

[52] U. Piomelli, E. Balaras, Wall layer models for large eddy simulation, Annual Review of Fluid Mechanics 34 (2002) 349–374.

[53] S. B. Pope, Turbulent Flows, Cambridge U. Press, 2000.

[54] U. Schumann, Subgrid scale model for finite difference simulations of turbulent flows in plane channels and annuli., Journal of Computational Physics 18 (1975) 376–404.

[55] S. Ghosal, P. Moin, The basic equations for the large eddy simulation of turbulent flows in complex geometry, Journal of Computational Physics 118 (1995) 24–37.

[56] S. Menon, W.-W. Kim, High Reynolds number flow simulations using the localized dynamic subgrid-scale model, AIAA Paper 96–0425 (1996).

[57] S. Menon, P.-K. Yeung, W.-W. Kim, Effect of subgrid models on the computed interscale energy transfer in isotropic turbulence, Computers and Fluids 25 (1996) 165–180.

[58] P. Moin, D. Carati, T. Lund, S. Ghosal, K. Akselvoll, Developments and applications of dynamic models for large eddy simulation of complex flows, in: AGARD Conference Proceedings 551, pp. 1–1–1–9.

[59] J. Bardina, J. Ferziger, W. Reynolds, Improved subgrid scale models for large eddy simulations, AIAA Paper 80–1357 (1980).

[60] B. Geurts, B. Vreman, H. Kuerten, Comparison of DNS and LES of transitional and turbulent compressible flow: flat plate and mixing layer, in: AGARD Conference Proceedings 551, pp. 5–1–5–14.

[61] S. Menon, P. K. Yeung, Analysis of subgrid models using direct and large-eddy simulations of isotropic turbulence, in: AGARD Conference Proceedings 551, pp. 10–1–10–12.

[62] M. Bassenne, J. Urzay, G. Park, P. Moin, Constant-energetics physical-space forcing methods for improved convergence to homogeneous-isotropic turbulence with application to particle-laden flows, Physics of Fluids 28 (2016) 035114.

[63] R. Hogan, J. Cuzzi, Stokes and Reynolds number dependence of preferential particle concentration in simulated three-dimensional turbulence, Physics of Fluids 13 (2001) 2938–2945.

[64] A. Scotti, C. Meneveau, A fractal method for large eddy simulation of turbulent flow, Physica D. 127 (1999) 198–232.

[65] J. C. H. Fung, J. C. R. Hunt, N. A. Malik, R. J. Perkins, Kinematic simulation of homogeneous turbulence by unsteady random Fourier modes, J. Fluid Mech. 236 (1992) 281–318.

[66] B. Vreman, B. Geurts, H. Kuerten, Subgrid-modelling in LES of compressible flows, Appl. Sci. Res. 54 (1995) 191–203.

[67] A. Putnam, Integratable form of droplet drag coefficient, Ars Journal 31 (1961) 1467–1468.

[68] M. Alletto, M. Breuer, Prediction of turbulent particle-laden flow in horizontal smooth and rough pipes inducing secondary flow, Int. J. Multiph. Flow 55 (2013) 80–98.

[69] D. Lilly, A proposed modification of the Germano subgrid-scale closure method, Phys. Fluids A 4 (1992) 633–635.

[70] V. Armenio, U. Piomelli, V. Fiorotto, Effect of the subgrid scales on particle motion, Physics of Fluids 11 (1999) 3030–3042.

[71] V. Sankaran, S. Menon, LES of spray combustion in swirling flows, Journal of Turbulence 3 (2002) 1–23.

[72] H. G. Weller, G. Tabor, H. Jasak, C. Fureby, A tensorial approach to computational continuum mechanics using object-oriented techniques, Computers in physics 12 (1998) 620–631.

[73] D. Mahida, E. Durant, P. Kumar, R. Ranjan, Study of airflow and aerosol deposition characteristics within human airways using large-eddy simulations, in: APS Division of Fluid Dynamics Meeting Abstracts, pp. H01–007.

[74] R. I. Issa, Solution of the implicitly discretised fluid flow equations by operator-splitting, Journal of computational physics 62 (1986) 40–65.

[75] S. V. Patankar, D. B. Spalding, A calculation procedure for heat, mass and momentum transfer in three-dimensional parabolic flows, in: Numerical prediction of flow, heat transfer, turbulence and combustion, Elsevier, 1983, pp. 54–73.

[76] G. B. Macpherson, N. Nordin, H. G. Weller, Particle tracking in unstructured, arbitrary polyhedral meshes for use in cfd and molecular dynamics, Communications in Numerical Methods in Engineering 25 (2009) 263–273.

[77] K. Yu, K. Lau, C. Chan, Numerical simulation of gas-particle flow in a single-side backward-facing step flow, J. Comput. Appl. Math. 163 (2004) 319–331.

[78] K. Mohanarangam, J. Tu, Two-fluid model for particle-turbulence interaction in a backward-facing step, AIChE 53 (2007) 22543–2264.

[79] Pointwise, https://www.pointwise.com/, 2020.

[80] C. Y. Lee, S. Cant, Assessment of LES Subgrid-scale Models and Investigation of Hydrodynamic Behaviour for an Axisymmetrical Bluff Body Flow, Flow Turbulence Combust. 98 (2017) 155–176.

[81] F. Greizfu, C. Kratzsch, T. Forgber, F. Lidner, R. Schwarze, Assessment of particle-tracking models for dispersed particle-laden flows implemented in OpenFOAM and ANSYS FLUENT, Eng. Appl. Comput. Fluid Mech. 10 (2015) 30–43.

[82] Tecplot, https://www.tecplot.com/, 2021.

PUBLICATIONS

The research leading up to this thesis has been presented at the UTC level and at the professional conference level, as described below:

- Johnston, T., Durant, E., & Ranjan, R. (2021). On the effects of subgrid dispersion in large-eddy simulation of particle-laden turbulent channel flow bounded by rough walls. Bulletin of the American Physical Society.
- Johnston, T. (2021). Effects of Subgrid-Scale Modeling on the Statistics of Wall-Bounded Separating/Reattaching Turbulent Flows. UTC College of Engineering and Computer Science.
- Johnston, T. (2021). Effects of Subgrid Dispersion Modeling on the Statistics of Particle-Laden Turbulent Separating/Reattaching Flows. ReSEARCH Dialogues 2021 Conference Proceedings.

VITA

Timothy Johnston was born in 1998 in Connecticut to Mr. Joseph Johnston and Mrs. Michele Rife. He attended the University of New Hampshire, where he studied mechanical engineering. During his undergraduate education, he led the controls team for the Formula SAE Design Competition as his senior capstone project. In May 2020, Timothy graduated with a Bachelor of Science in Mechanical Engineering. In August of that same year, he was accepted to The Graduate School at the University of Tennesse at Chattanooga to continue his education in mechanical engineering. During his graduate studies, he has researched modeling and simulation of particle-laden turbulent flows under the supervision of Dr. Reetesh Ranjan. In December 2021, Timothy graduated from the University of Tennessee at Chattanooga with a Master of Science in Mechanical Engineering.